Exploring muonphilic dark matter with the Z_2 -even mediator at muon colliders

Wanyun Chen^{1,2}, Haoqi Li¹, Chih-Ting Lu^{1,3}, Qiulei Wang¹

- ¹ Department of Physics and Institute of Theoretical Physics, Nanjing Normal University, Nanjing, 210023, P. R. China
- ² Department of Physics, Konkuk University, 120 Neungdong-ro, Gwanqjin-qu, Seoul 05029, Republic of Korea and
- ³ Nanjing Key Laboratory of Particle Physics and Astrophysics, Nanjing, 210023, China

Abstract

The Galactic Center GeV Excess (GCE) remains a compelling but enigmatic signal from the inner region of our galaxy. Muonphilic dark matter (DM), which couples exclusively to muons via a new mediator, provides a viable explanation for the GCE and relic density while naturally evading constraints from direct detection, collider searches and other multi-messenger observations. Based on the viable non-resonant parameter space identified in previous global fits, we perform a comprehensive study exploring the prospects for discovering such muonphilic DM in the context of a future 3 TeV muon collider, focusing on simplified models with a Z_2 -even mediator. Three distinct search strategies are investigated: visible on-shell mediator decays ($\mu^+\mu^-\gamma$ final state), invisible on-shell mediator decays (mono-photon plus missing energy), and mono-photon production via off-shell mediators. Through a detailed signal-background analysis using cut-and-count methods, we project the exclusion limits at 95% confidence level for seven representative models across a wide range of mediator masses. Our results demonstrate that the projected limits cover a significant portion of the viable parameter space that explains the GCE, establishing a muon collider as a decisive machine for testing the muonphilic DM hypothesis.

I. INTRODUCTION

Dark matter (DM) is a non-luminous form of matter that does not interact electromagnetically, yet its gravitational influence profoundly shapes the dynamics of galaxies and large-scale structures in the universe [1, 2]. As one of the most compelling pieces of evidence for physics beyond the Standard Model (SM), the existence of DM remains a major challenge to modern physics [3, 4]. Although DM constitutes approximately 27% of the total mass-energy content of the universe, compared to merely 5% from ordinary baryonic matter, its particle nature remains entirely unknown [5–9]. Long-standing anomalies in indirect DM detection, such as the galactic center GeV excess (GCE) [10–12], the antiproton excess [13–15], and the 511 keV [16–18] and 3.5 keV [10, 19] lines, have motivated extensive efforts to uncover potential connections to DM physics.

Among these indirect detection signals, the GCE, first identified by the Fermi-LAT satellite in 2009 [20–22, 25], remains one of the most persistent and challenging puzzles in highenergy astrophysics and particle physics. This signal exhibits a significant gamma-ray excess in the 1–3 GeV range from the galactic center, with a spatial distribution consistent with the predicted NFW density profile of DM [26]. Its spectral shape also closely resembles expectations from weakly interacting massive particle (WIMP) annihilation channels, such as $b\bar{b}$ [21, 22]. However, secondary particles (e.g., hadrons or electrons) produced in such annihilations would generate observable signals at other wavelengths (e.g., radio or X-rays), though current multi-wavelength observations have not yet confirmed such counterparts [23, 24].

Various DM models have been proposed to explain the GCE [27–40, 46, 47]. Among these, muonphilic DM has emerged in recent years as a promising candidate due to its consistency with multi-messenger observational constraints [12, 40]. Conventional WIMP models, which remain leading explanations, typically involve annihilation into SM particles (e.g., $b\bar{b}$, $\tau^+\tau^-$, or W^+W^-), producing gamma rays via inverse Compton scattering or hadronization processes. However, many such models face tensions with antiproton and positron spectra from AMS-02 [48, 49] and direct detection limits from experiments such as PandaX [50].

To resolve these tensions, muonphilic DM models have been proposed. These posit that DM couples exclusively to muon pairs ($\mu^+\mu^-$) via a mediator, with negligible interactions with other SM particles [40, 51–64]. This feature avoids hadronic or electronic secondary emission, offering a consistent explanation for the GCE without conflicting with other ob-

servational data. When DM particles annihilate into $\mu^+\mu^-$ or produce four muons via the decays from a pair of mediators, final-state radiation (FSR) photons are generated predominantly in the 1–5 GeV range. The resulting spectrum exhibits a pronounced peak-like feature that aligns well with the GCE observed by Fermi-LAT [12, 40]. Compared to other channels (e.g., $b\bar{b}$), the $\mu^+\mu^-$ final state yields a harder FSR spectrum with a steeper rise and sharper peak around 1–3 GeV, making it ideal for reproducing the GCE spectral morphology [41, 42]. Furthermore, since the model couples only to muons, it avoids detectable synchrotron radiation from electrons/positrons or hadronic emission, thereby evading constraints from radio (e.g., WMAP/Planck synchrotron limits) and X-ray (e.g., Chandra inverse Compton bounds) observations [43–45]. This enables muonphilic DM models to resolve persistent multi-messenger tensions that challenge conventional DM scenarios.

In muonphilic DM models, DM couples exclusively to muons via a mediator, such as a dark photon or scalar boson, making it challenging to probe at conventional colliders like the Large Hadron Collider (LHC) and Large Electron-Positron Collider (LEP) as well as direct detection experiments, which consequently impose weak constraints. However, owing to the muon's mass (approximately 200 times that of the electron) and its absence from strong interactions, a high-energy muon collider (at the TeV scale) offers superior energy resolution and cleaner backgrounds compared to hadron colliders (e.g., LHC) or electron-positron colliders (e.g., CEPC/FCC-ee) [65–67]. Thus, high-energy muon colliders represent a promising avenue for directly probing muonphilic DM¹.

In this work, we investigate the following signal processes at a muon collider: (1) Visible on-shell mediator decays: $\mu^+\mu^- \to \gamma + \text{MED}$, with MED $\to \mu^+\mu^-$, where MED denotes the mediator; (2) Mono-photon with on-shell mediators: $\mu^+\mu^- \to \gamma + \text{MED}$, with MED $\to \chi\bar{\chi}$, where the DM particles (χ) yield missing energy and the photon energy distribution exhibits a peak-like structure; (3) Mono-photon with off-shell mediators: $\mu^+\mu^- \to \gamma + \chi\bar{\chi}$, producing photon and missing energy signatures similar to SM backgrounds, thereby complicating signal extraction. Using these search strategies, a muon collider can directly test whether muonphilic DM models resolve the longstanding GCE, precisely measure the DM-muon coupling strength and mediator mass, and complement the limitations of LHC searches and direct detection experiments. Combined with astrophysical observations from Fermi-LAT,

¹ While several proposals exist to test DM models relevant to the GCE at colliders (see Ref. [28–32, 37, 68–71]), to the best of our knowledge, none have explored muonphilic DM models motivated by the GCE in the context of a muon collider, as investigated in this work.

AMS-02, and others, muon collider searches enable cross-validation of potential DM-induced astrophysical signals.

The rest of this paper is organized as follows: Sec. II briefly reviews the simplified muon-philic DM models considered and their key parameter space. Based on the allowed parameter space of muonphilic DM models, Sec. III proposes three search strategies and provides a state-of-the-art signal-background analysis. The resulting projected exclusion limits for muonphilic DM models at muon colliders are presented and discussed in Sec. IV. Finally, we conclude in Sec. V.

II. SIMPLIFIED MUONPHILIC DM MODELS WITH THE \mathbb{Z}_2 -EVEN MEDIATOR

A. The models

For simplified muonphilic DM models consisting of a Standard Model (SM) singlet DM particle and a mediator (MED), our previous work [40] systematically introduced all renormalizable interaction types: 16 in the Z_2 -even mediator framework and 7 in the Z_2 -odd mediator framework. These models are constructed from different spin and interaction combinations of the DM and MED particles, with DM stability ensured by the Z_2 symmetry. Using a likelihood function incorporating experimental observations, including the Fermi-LAT GCE [42], Plank DM relic density [72], PandaX-4T direct detection limits [73], LEP collider bounds [74], and the muon g-2 anomaly δa_{μ} [75], we performed a global analysis of all 23 interaction types to exclude parameter spaces inconsistent with observational data.

In Z_2 -even mediator models, interactions between DM pairs and SM muon pairs are mediated by a Z_2 -even SM singlet mediator with spin 0 or 1. Such muonphilic DM models naturally evade LEP and LHC constraints from mono-photon and mono-jet searches [76, 77], thus allowing for the existence of DM at the electroweak scale. Based on the spin and interaction types of DM and MED, the 16 Z_2 -even interactions can be categorized into three major classes: (1) fermionic DM (χ) models; (2) scalar DM (S) models; (3) vector DM (S_2) models. When the DM mass (S_2) is less than the mediator mass (S_2), S_2 0, the observed relic density can only be achieved through the S_2 1 final state. For S_2 2 final producing a S_2 4 final process DM+DM S_2 4 mediator mass (S_2 5 mediator mass (S_2 6 mediator mass (S_2 7 mediator mass (S_2 8 mediator mass (S_2 9 mediator

state. However, explaining the GCE in this case requires a significantly larger annihilation cross-section that typically conflicts with relic density constraints.

 Z_2 -even mediator models benefit from their ability to modulate early-time and present-day DM annihilation rates through s-channel resonance enhancement mechanism ($M \approx 2m_D$), preserving the relic density while enhancing the GCE signal. For example, scalar mediator models (\mathcal{L}_3 , \mathcal{L}_9 , \mathcal{L}_{13}) can simultaneously satisfy relic density ($\langle \sigma v \rangle \approx 3 \times 10^{-26} \text{ cm}^3/\text{s}$) [72] and the GCE signal ($\langle \sigma v \rangle \approx 4 \times 10^{-26} \text{ cm}^3/\text{s}$) [42] requirements by tuning the mediator decay width Γ_{MED} , while also explaining the muon g-2 anomaly ($\delta a_{\mu} \approx 2.51 \times 10^{-9}$) [75]. Moreover, the DM-nucleon scattering cross-sections are suppressed to $\sigma_{\text{SI}} \sim 10^{-48} \text{ cm}^2$ due to two-loop processes, evading current direct detection limits.

In contrast, Z_2 -odd mediator models feature t-channel dominated DM annihilation. Since the mediator mass always exceeds the DM mass, the only accessible final state is 2μ , precluding the resonant enhancement mechanism available Z_2 -even mediator models. This makes it challenging to simultaneously explain both the GCE and DM relic abundance. Additionally, the electrically charged nature of the mediator subjects it to LEP mass limits $(M>103.5~{\rm GeV})$ [74], significantly constraining the viable parameter space [40]. Satisfying the relic density requirement necessitates strong couplings $(g_D>1)$, which typically cause DM-nucleon scattering cross-sections to exceed current limits $(\sigma_{\rm SI}>10^{-46}~{\rm cm}^2)$ [73]. In the end, the only Z_2 -odd mediator model that marginally survives under thermal DM production is the vector DM model \mathcal{L}_{23} $(g_D\bar{\psi}\gamma^{\mu}P_R\mu X_{\mu}^{\dagger})$, but it requires $M>300~{\rm GeV}$ and $g_D>1.5$ to achieve the observed DM relic density. The parameter space is readily testable by LHC Run-3 data. Consequently, Z_2 -odd mediator models possess essentially no viable parameter space under current GCE, relic density, and direct detection constraints, while Z_2 -even mediator models still retain viable regions in both resonance and non-resonance regimes.

	Scalar	Fermion	Vector
Dark Matter	S	χ	X^{μ}
Mediator	ϕ	ψ	V^{μ}

TABLE I: The dark matter and mediator notations used in this work.

This work focuses on \mathbb{Z}_2 -even mediator models. The notations for relevant DM and MED

Types	Lagrangian
ay and d	$\mathcal{L}_3 = (g_D \bar{\chi} i \gamma^5 \chi + g_f \bar{f} f) \phi$
χ and ϕ	$\mathcal{L}_4 = (g_D \bar{\chi} i \gamma^5 \chi + g_f \bar{f} i \gamma^5 f) \phi$
χ and V_{μ}	$\mathcal{L}_8 = (g_D \bar{\chi} \gamma^\mu \chi + g_f \bar{f} \gamma^\mu \gamma^5 f) V_\mu$
C 1 1	$\mathcal{L}_9 = (M_{D\phi} S^{\dagger} S + g_f \bar{f} f) \phi$
$S \text{ and } \phi$	$\mathcal{L}_{10} = (M_{D\phi}S^{\dagger}S + g_f\bar{f}i\gamma^5f)\phi$
V 1 1	$\mathcal{L}_{13} = (M_{D\phi} X^{\mu} X^{\dagger}_{\mu} + g_f \bar{f} f) \phi$
X_{μ} and ϕ	$\mathcal{L}_{14} = (M_{D\phi} X^{\mu} X^{\dagger}_{\mu} + g_f \bar{f} i \gamma^5 f) \phi$

TABLE II: The Lagrangian of relevant dark matter simplified models in the Z_2 -even mediator scenario. Here g_D and $M_{D\phi}$ are relevant couplings between the mediator and a pair of DM particles with dimensionless and dimension-1, respectively. Similarly, g_f is the dimensionless coupling between the mediator and a pair of muons.

candidates with various spin assignments are summarized in Table I. We specifically explore non-resonance regions of these muonphilic DM models at 3 TeV muon colliders [65]. The resonance regions are highly fine-tuned and sensitive to slight parameter variations within narrow parameter spaces, requiring specialized analysis that we defer to future work. Based on Table II and Figure 3 of Ref. [40], we select simplified DM models (\mathcal{L}_3 , \mathcal{L}_4 , \mathcal{L}_8 , \mathcal{L}_9 , \mathcal{L}_{10} , \mathcal{L}_{13} , \mathcal{L}_{14}) with non-resonant parameter regions, collecting them in Table II. Here g_D and $M_{D\phi}$ are relevant couplings between the mediator and a pair of DM particles with dimensionless and dimension-1, respectively. Similarly, g_f is the dimensionless coupling between the mediator and a pair of muons. Detailed expressions for DM annihilation cross-sections and DM-nucleon scattering cross-sections are provided in our previous work [40].

B. The predicted parameter space

According to global fits in Ref. [40], only the simplified muonphilic DM models, \mathcal{L}_3 , \mathcal{L}_4 , \mathcal{L}_8 , \mathcal{L}_9 , \mathcal{L}_{10} , \mathcal{L}_{13} , and \mathcal{L}_{14} , exhibit allowed parameter space outside resonance regions². The parameter space can be further divided into two scenarios: $M > 2m_D$ and $M < 2m_D$. For $M > 2m_D$, on-shell mediator production is possible at muon colliders if kinematically

 $^{^2}$ Here we do not consider the \mathcal{L}_6 case, as it only permits very light mediators outside the resonance region.

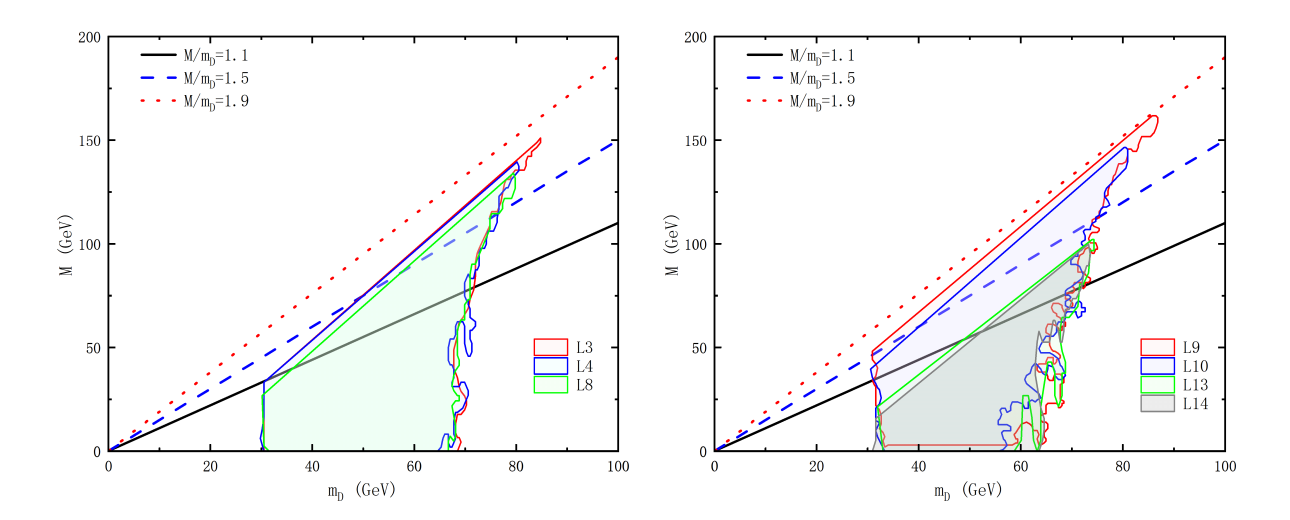


FIG. 1: The parameter space for relevant simplified muonphilic DM models with $M < 2m_D$, based on Ref. [40], is shown here. The left panel depicts \mathcal{L}_3 , \mathcal{L}_4 and \mathcal{L}_8 , while the right panel covers \mathcal{L}_9 , \mathcal{L}_{10} , \mathcal{L}_{13} and \mathcal{L}_{14} . For comparison, three benchmark ratios of mediator to DM mass are displayed: $M/m_D = 1.1$ (black-solid), $M/m_D = 1.5$ (blue-dashed) and $M/m_D = 1.9$ (red-dotted).

accessible. The mediator may subsequently decay into either a DM particle pair or a muon pair, depending on the branching ratios. In contrast, for $M < 2m_D$, the mediator decays exclusively to muon pairs. DM particle pairs can only be produced via off-shell mediators, making their detection more challenging and strongly dependent on the ratio M/m_D . We therefore present this ratio for the relevant DM models in Fig. 1, based on results from Ref. [40]. We observe that only models \mathcal{L}_9 and \mathcal{L}_{10} feature parameter space near $M/m_D = 1.9$. The parameter spaces of \mathcal{L}_3 , \mathcal{L}_4 , and \mathcal{L}_8 approach the ratio $M/m_D = 1.5$, while \mathcal{L}_{13} and \mathcal{L}_{14} exhibit relatively small regions near $M/m_D = 1.1$. Note that for a very light mediator (where $M/m_D \ll 1$), direct searches for visible on-shell mediator decays are more efficient in fixed-target experiments than in muon colliders.

We consider the following three search strategies for probing muonphilic DM models at muon colliders in this work:

• Visible on-shell mediator decays

The mediator is produced on-shell at muon colliders and subsequently decays to a muon pair: $\mu^+\mu^- \to \gamma$, MED $\to \gamma(\mu^+\mu^-)$. The production cross-section depends only

on g_f :

$$\sigma(\mu^+\mu^- \to \gamma, \text{MED}) \propto g_f^2,$$
 (1)

while the branching ratio $\mathcal{B}(\text{MED} \to \mu^+\mu^-)$ is a function of g_f , g_D , and m_D .

Invisible on-shell mediator decays

We consider the mono-photon signature in the regime where $M > 2m_D$ with $m_D < 100$ GeV, and where the couplings satisfy $g_D \cdot g_f \gtrsim 10^{-2}$ for models \mathcal{L}_3 , \mathcal{L}_4 , and \mathcal{L}_8 , or $M_{D\phi} \cdot g_f \gtrsim 10^{-4}$ TeV for models \mathcal{L}_9 , \mathcal{L}_{10} , \mathcal{L}_{13} , and \mathcal{L}_{14} .

Mono-photon with off-shell mediators

We study the parameter region where $1.1m_D \lesssim M \lesssim 1.9m_D$ with $m_D < 100$ GeV, and with coupling constraints $g_D \cdot g_f \gtrsim 10^{-2}$ for \mathcal{L}_3 , \mathcal{L}_4 , \mathcal{L}_8 , and $M_{D\phi} \cdot g_f \gtrsim 10^{-4}$ TeV for \mathcal{L}_9 , \mathcal{L}_{10} , \mathcal{L}_{13} , and \mathcal{L}_{14} .

III. MUONPHILIC DM SEARCH STRATEGIES AT MUON COLLIDERS

Based on the structure of parameter space, we develop three distinct search strategies for muonphilic DM models at muon colliders: Visible on-shell mediator decays, Sec. III A; Invisible on-shell mediator decays, Sec. III B; Mono-photon signatures with off-shell mediators, Sec. III C. In the following subsections, we employ the following computational pipeline: FeynRules [78] generates UFO model files for the Lagrangians listed in Table II; MadGraph5_aMC@NLO [79] produces Monte Carlo events for signal and background hard processes; Pythia8 [80] handles parton showering and hadronization; and Delphes3 [81] with a muon collider template performs fast detector simulation.

A. Visible on-shell mediator decays

Figure 3 in Ref. [40] indicates allowed parameter spaces exist outside resonance regions for models \mathcal{L}_3 , \mathcal{L}_4 , \mathcal{L}_8 , \mathcal{L}_9 , \mathcal{L}_{10} , \mathcal{L}_{13} , and \mathcal{L}_{14} . However, when considering on-shell mediator production through the visible decay channel $\mu^+\mu^- \to \gamma \text{MED}$ followed by MED $\to \mu^+\mu^-$, only three interaction types for the mediators and a pair of muons emerge: scalar (\mathcal{L}_3 , \mathcal{L}_9 , \mathcal{L}_{13}), pseudoscalar (\mathcal{L}_4 , \mathcal{L}_{10} , \mathcal{L}_{14}), and axial-vector (\mathcal{L}_8). For the proposed 3 TeV muon collider, we focus on mediator masses M < 1.5 TeV, covering all upper bounds of mediator masses

in these models except \mathcal{L}_9 and \mathcal{L}_{10} , where M may reach 3 TeV. Our search strategies remain extensible to heavier mediators for higher-energy muon colliders.

Cut description		background	signal1	signal2	signal3	signal4
	Cross-section [fb]	179	22.66	30.87	34.20	39.79
Cut-1	$N(\gamma), \ N(\mu^+), \ N(\mu^-) > 0,$	0.82	0.78	0.85	0.84	0.83
	$E(\gamma), \ p_T(\mu^{\pm}) > 20 \text{GeV},$					
	$ \eta(\gamma) ,\ \eta(\mu^\pm) <2.5$					
Cut-2	$E(\gamma) > 150 \mathrm{GeV},$	0.19	0.54	0.65	0.62	0.61
	$ \eta(\gamma) < 1.8$					
Cut-3	$p_T(\mu^{\pm}) > 150 \text{GeV},$	0.08	0.41	0.53	0.51	0.51
	$ \eta(\mu^\pm) <1.6$					
Cut-4	$\Delta R(\mu^+\mu^-) < 3.0$	0.01	0.24	0.40	0.46	0.45
Cut-5	$ M(\mu^+\mu^-) - M < 0.15M$	2×10^{-3}	0.23	0.39	0.44	0.43

TABLE III: The cut-flow table for visible on-shell mediator decays of the \mathcal{L}_3 model and its relevant background. The four benchmark points are signal-1 ($M=50~{\rm GeV}$), signal-2 ($M=500~{\rm GeV}$), signal-3 ($M=900~{\rm GeV}$), signal-4 ($M=1300~{\rm GeV}$).

In this subsection, we demonstrate our methodology using the \mathcal{L}_3 and \mathcal{L}_8 models, presenting benchmark points (BPs), kinematic distributions, and event selection criteria. The analysis for other models is presented in Sec. IV. Note that for $M > 2m_D$, kinematically allowed invisible mediator decays lead to model-dependent variations in the MED $\to \mu^+\mu^-$ branching ratios. Therefore, we set the mass ratio $M/m_D = 2.5$ and fix the coupling constant ratio for each model, thereby ensuring that the branching ratio of MED $\to \mu^+\mu^-$ is no less than 99%. Four benchmark mediator masses are considered in this study: (1) Signal-1: M = 50 GeV; (2) Signal-2: M = 500 GeV; (3) Signal-3: M = 900 GeV; (4) Signal-4: M = 1300 GeV. For the \mathcal{L}_3 model, the benchmark coupling parameters are set to $g_f = 0.2$ and $g_D = 0.025$, corresponding to a coupling constant ratio of $g_D/g_f = 1/8$; For the \mathcal{L}_8 model, the benchmark coupling parameters are set to $g_f = 0.225$, with the corresponding constant ratio being $g_D/g_f = 1/9$. For the signal process $\mu^+\mu^- \to \gamma$ MED with MED $\to \mu^+\mu^-$, the irreducible SM background process is $\mu^+\mu^- \to \mu^+\mu^-\gamma$. The corresponding production cross-sections for the four BPs and the SM background are listed in

	Cut description	background	signal1	signal2	signal3	signal4
	Cross-section [fb]	179	49.84	62.90	71.43	86.97
Cut-1	$N(\gamma), \ N(\mu^+), \ N(\mu^-) > 0,$	0.82	0.77	0.85	0.84	0.83
	$E(\gamma), \ p_T(\mu^{\pm}) > 20 \text{GeV},$					
	$ \eta(\gamma) , \ \eta(\mu^{\pm}) < 2.5$					
Cut-2	$E(\gamma) > 150 \mathrm{GeV},$	0.19	0.53	0.60	0.59	0.58
	$ \eta(\gamma) < 1.8$					
Cut-3	$p_T(\mu^{\pm}) > 150 \text{GeV},$	0.08	0.40	0.47	0.46	0.48
	$ \eta(\mu^{\pm}) <1.6$					
Cut-4	$\Delta R(\mu^+\mu^-) < 3.0$	0.01	0.20	0.32	0.40	0.41
Cut-5	$ M(\mu^+\mu^-) - M < 0.15M$	2×10^{-3}	0.19	0.30	0.38	0.40

TABLE IV: Similar to Table III, but for the \mathcal{L}_8 model.

the second row of Tables III and IV. Representative kinematic distributions for signal and background processes are shown in Fig. 2.

We find that the peak of the background photon energy $E(\gamma)$ appears at 50 GeV, whereas the peaks for the four signal BPs occur at higher energies and decrease with increasing mediator mass, as shown in the top-left panel of Fig. 2. The photon pseudorapidity $\eta(\gamma)$ for the background and the light mediator case (signal-1) displays a pronounced forward-backward distribution. However, this behavior does not appear for heavier mediators, resulting in a flatter $\eta(\gamma)$ distribution (top-right panel). A similar forward-backward distribution is also observed in the $\eta(\mu^{\pm})$ variable for both the background and signal-1 (middle-left panel). The transverse momentum distribution $p_T(\mu^-)$ peaks around 350 GeV for the background. For the signal processes, a heavier mediator leads to a harder $p_T(\mu^-)$ spectrum (middle-right panel). The opening angle distribution $\Delta R(\mu^+\mu^-)$ provides a key distinction: a light mediator (signal-1) is produced with a large boost, leading to a smaller $\Delta R(\mu^+\mu^-)$ compared to the background. The background exhibits a significantly larger $\Delta R(\mu^+\mu^-)$ than all four signal BPs (bottom-left panel). Finally, the dimuon invariant mass distributions $M(\mu^+\mu^-)$ for the signals peak at their respective mediator masses, while the background distribution is broad and featureless (bottom-right panel).

Based on the above analysis of kinematic distributions, the following event selection

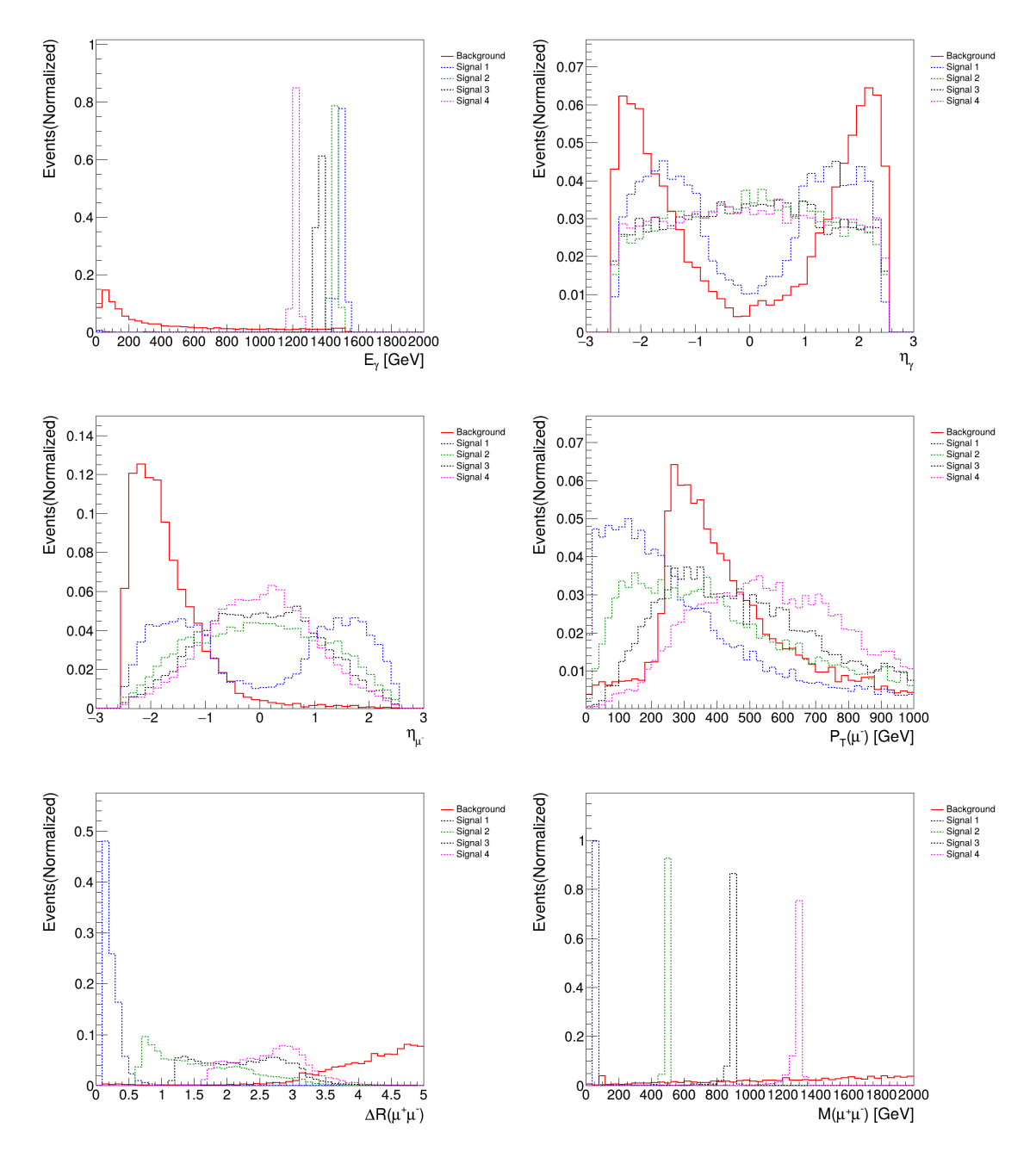


FIG. 2: Visible on-shell mediator decays of the \mathcal{L}_3 model, representative kinematic distributions include photon energy $E(\gamma)$ (top-left), photon pseudorapidity $\eta(\gamma)$ (top-right), μ^- transverse momentum $p_T(\mu^-)$ (middle-left), μ^- pseudorapidity $\eta(\mu^-)$ (middle-right), ΔR of a muon pair (bottom-left), and invariant mass $M(\mu^+\mu^-)$ of a muon pair (bottom-right) for signal-1 (M=50 GeV, blue-dotted line), signal-2 (M=500 GeV, green-dotted line), signal-3 (M=900 GeV, black-dotted line), signal-4 (M=1300 GeV, purple-dotted line) and background (red-solid line).

criteria for signal and background events are adopted:

- Cut-1 (basic cuts): $N(\gamma)$, $N(\mu^+)$, $N(\mu^-) > 0$, with leading photon, a pair of muons satisfying $E(\gamma)$, $p_T(\mu^{\pm}) > 20 \,\text{GeV}$, and $|\eta(\gamma)|$, $|\eta(\mu^{\pm})| < 2.5$;
- Cut-2: $E(\gamma) > 150 \,\text{GeV}$, and $|\eta(\gamma)| < 1.8$;
- Cut-3: $p_T(\mu^{\pm}) > 150 \,\text{GeV}$, and $|\eta(\mu^{\pm})| < 1.6$;
- Cut-4: $\Delta R(\mu^+\mu^-) < 3.0;$
- Cut-5: $|M(\mu^+\mu^-) M| < 0.15M$.

After applying these selection criteria, the signal and background efficiencies are calculated. Tables III and IV summarize the selection efficiencies for the four BPs in the \mathcal{L}_3 and \mathcal{L}_8 models, respectively. The final background efficiency is suppressed to $\mathcal{O}(10^{-3})$, while the signal efficiencies remain above 19% and can exceed 40% for larger mediator masses.

B. Invisible on-shell mediator decays

In this context, global fitting results from Fig. 3 of Ref. [40] show $M > 2m_D$ with $m_D < 100$ GeV. With the exception of models \mathcal{L}_9 and \mathcal{L}_{10} , where the mediator masses M can reach upper bounds of 3 TeV, all other models $(\mathcal{L}_3, \mathcal{L}_4, \mathcal{L}_8, \mathcal{L}_{13}, \mathcal{L}_{14})$ exhibit upper bounds of M below 1.5 TeV. Given our focus on the 3 TeV muon collider proposal, we restrict our study to mediator masses $M \lesssim 1.5$ TeV. Notably, on-shell mediator production via muon pairs occurs through scalar-type couplings $(\mathcal{L}_3, \mathcal{L}_9, \mathcal{L}_{13})$, pseudoscalar-type couplings $(\mathcal{L}_4, \mathcal{L}_{10}, \mathcal{L}_{14})$, or axial-vector-type couplings (\mathcal{L}_8) . However, branching ratios for mediator decays to DM particle pairs vary across models due to their distinct interaction types.

To demonstrate our search methodology, we use the \mathcal{L}_3 model as a representative example, presenting BPs, kinematic distributions, and event selection criteria. The analysis is subsequently extended to other models. We select four mediator masses: Signal-1 (M=50 GeV), signal-2 (M=500 GeV), signal-3 (M=900 GeV), and signal-4 (M=1300 GeV), with a fixed mediator-to-DM mass ratio $M/m_D=2.5$, and choose $g_D=1.5$ and $g_f=0.1$ as our benchmark couplings. The signal process is $\mu^+\mu^- \to \phi\gamma$, followed by the on-shell mediator decay to a pair of DM particles ($\phi \to \chi \bar{\chi}$). The irreducible SM background process is $\mu^+\mu^- \to \nu\bar{\nu}\gamma$. The corresponding production cross-sections for the four BPs and

Cut description		background	signal1	signal2	signal3	signal4
Cross-section [fb]		2980	8.357	8.634	9.378	11.16
	$N(\gamma) > 0$	0.92	0.91	0.91	0.91	0.91
Cut-1	$E(\gamma) > 100 \text{GeV} \& \eta(\gamma) < 2.5$	0.35	0.91	0.91	0.91	0.91
	$E_T > 40\mathrm{GeV}$	0.30	0.91	0.91	0.91	0.91
Cut-2	$E(\gamma) > 1200 \mathrm{GeV}$	7.4×10^{-3}	0.91	0.91	0.91	0.83
Cut-3	$P_T(\gamma)/E > 0.4$	1.7×10^{-3}	0.57	0.56	0.51	0.38
Cut-4	$M_T > 1600 \mathrm{GeV}$	1.0×10^{-3}	0.45	0.45	0.42	0.32

TABLE V: The cut-flow table for the invisible on-shell mediator decay scenario $(M/m_D=2.5)$ of the \mathcal{L}_3 model and its relevant background. The four benchmark points are signal-1 $(M=50~{\rm GeV})$, signal-2 $(M=500~{\rm GeV})$, signal-3 $(M=900~{\rm GeV})$, signal-4 $(M=1300~{\rm GeV})$.

the SM background are listed in the second row of Table V. The representative kinematic distributions for signal and background processes are shown in Fig. 3.

For on-shell mediator production with an initial state radiation (ISR) photon, the photon energy $E(\gamma)$ exhibits a monochromatic peak, while the background $E(\gamma)$ distribution decreases smoothly, as shown in the top-left panel of Fig. 3. The transverse missing energy E_T is more energetic for signals than for background (top-right panel). Conversely, the missing energy E distribution shows the opposite trend to $E(\gamma)$ distribution (bottom-left panel). Finally, since the photon transverse momentum and missing energy distributions differ significantly between signals and background, we examine the ratio $P_T(\gamma)/E$ distribution (bottom-right panel) to enhance discrimination.

Based on these kinematic distributions, we implement the following event selections to signal and background events:

- Cut-1 (basic cuts): $N(\gamma) > 0$, with the leading photon satisfying $E(\gamma) > 100\,\text{GeV}$ and $|\eta(\gamma)| < 2.5$, plus $E_T > 40\,\text{GeV}$;
- Cut-2: $E(\gamma) > 1200 \,\text{GeV};$
- Cut-3: $P_T(\gamma)/E > 0.4$;

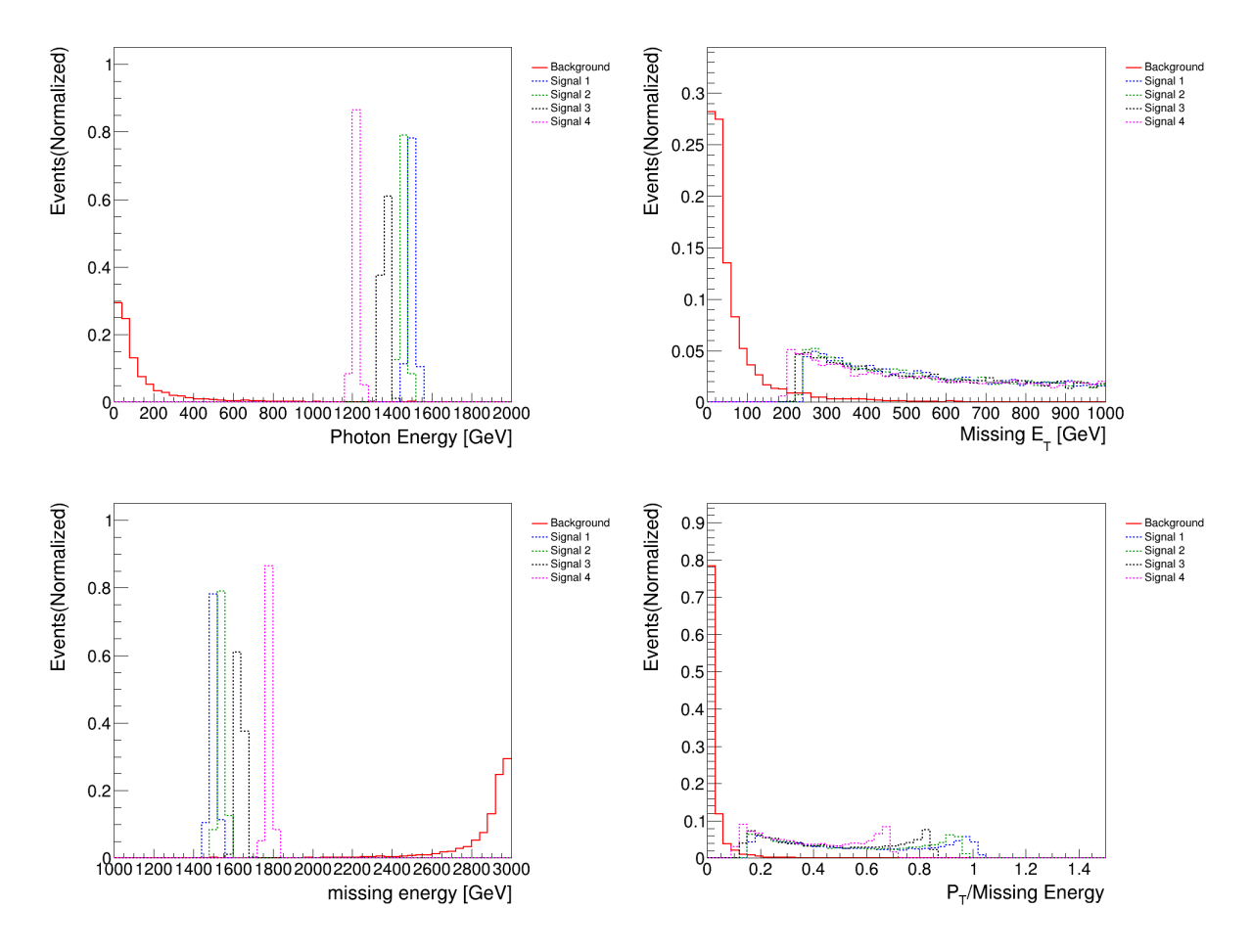


FIG. 3: In the invisible on-shell mediator decay scenario $(M/m_D = 2.5)$ of the \mathcal{L}_3 model, representative kinematic distributions include photon energy $E(\gamma)$ (top-left), missing transverse energy E_T (top-right), missing energy E (bottom-left), and the ratio of $P_T(\gamma)/E$ (bottom-right) for signal-1 (M = 50 GeV), blue-dotted line), signal-2 (M = 500 GeV), green-dotted line), signal-3 (M = 900 GeV), black-dotted line), signal-4 (M = 1300 GeV), purple-dotted line) and background (red-solid line).

• Cut-4: $M_T > 1600$ GeV, where the transverse mass for the mono-photon plus E_T is defined as

$$M_T = \sqrt{2P_T(\gamma) \cdot \cancel{E}_T \cdot (1 - \cos \Delta \phi)}, \tag{2}$$

with $\Delta \phi$ being the azimuthal angle between the leading photon and E_T .

Here, the final M_T selection is used to further distinguish signal and background events. Table V summarizes the selection efficiencies for four signal BPs in the \mathcal{L}_3 model and background. As efficiency table for the \mathcal{L}_4 model closely resemble to the \mathcal{L}_3 model's, we show

Cut description		background	signal1	signal2	signal3	signal4
Cross-section [fb]		2980	13.13	13.73	15.25	18.48
Cut-1	$N(\gamma) > 0$	0.92	0.91	0.91	0.91	0.91
	$E(\gamma) > 100 \text{GeV} \& \eta(\gamma) < 2.5$	0.35	0.91	0.91	0.91	0.91
	$E_T > 40\mathrm{GeV}$	0.30	0.91	0.91	0.91	0.91
Cut-2	$E(\gamma) > 1200 \mathrm{GeV}$	7.4×10^{-3}	0.91	0.91	0.91	0.83
Cut-3	$P_T(\gamma)/E > 0.4$	1.7×10^{-3}	0.50	0.49	0.47	0.34
Cut-4	$M_T > 1600 \mathrm{GeV}$	1.0×10^{-3}	0.37	0.37	0.36	0.29

TABLE VI: Similar to Table V, but for the \mathcal{L}_8 model.

only the \mathcal{L}_8 model in Table VI. Here we adopt the benchmark couplings of $g_D = 1.2$ and $g_f = 0.1$ in the \mathcal{L}_8 model.

C. Mono-photon signature with off-shell mediator

In regions of parameter space where $M < 2m_D$ for models \mathcal{L}_3 , \mathcal{L}_4 , \mathcal{L}_8 , \mathcal{L}_9 , \mathcal{L}_{10} , \mathcal{L}_{13} , \mathcal{L}_{14} , visible on-shell mediator decays provide optimal search sensitivity. However, when couplings to DM particles significantly exceed those to muon pairs, mono-photon signatures with offshell mediators offer complementary probes. We therefore investigate this situation through the off-shell mediator mono-photon channel. DM masses are constrainted to $m_D < 100 \text{ GeV}$ from global fitting results [40]. We consider three mediator-to-DM mass ratios: $M/m_D = \{1.1, 1.5, 1.9\}$ as mentioned in Sec. II B. To demonstrate our methodology, we select three representative models: \mathcal{L}_3 , \mathcal{L}_9 , and \mathcal{L}_{13} , presenting their BPs, kinematic distributions and event selection criteria before generalizing to other models in Sec. IV.

We select two representative DM masses, $m_D = 20$ and 100 GeV, with three benchmark mediator-to-DM mass ratio: (1) Signal-1: $M/m_D = 1.1$; (2) Signal-2: $M/m_D = 1.5$; (3) Signal-3: $M/m_D = 1.9$ for each scenario. The benchmark couplings are: $g_D = 0.5$, $g_f = 0.1$ for the \mathcal{L}_3 model; $M_{D\phi} = 100$ GeV, $g_f = 0.1$ for the \mathcal{L}_9 model; and $M_{D\phi} = 10$ GeV, $g_f = 0.1$ for the \mathcal{L}_{13} model. Taking the \mathcal{L}_3 model as an example, the signal process is $\mu^+\mu^- \to \chi\bar{\chi}\gamma$ via off-shell mediator ϕ , with irreducible SM background process $\mu^+\mu^- \to \nu\bar{\nu}\gamma$. The corresponding production cross-sections are listed in the second row of Tables VII-XII

	Cut description	background	signal1	signal2	signal3
	Cross-section [fb]	2980	0.42	0.45	0.53
	$N(\gamma) > 0$	0.92	0.91	0.91	0.91
Cut-1	$E(\gamma) > 100 \text{GeV} \& \eta(\gamma) < 2.5$	0.35	0.75	0.75	0.78
	$E_T > 40\mathrm{GeV}$	0.30	0.73	0.73	0.76
Cut-2	$E(\gamma) > 1200 \mathrm{GeV}$	7.4×10^{-3}	0.41	0.43	0.51
Cut-3	$P_T(\gamma)/E > 0.4$	1.7×10^{-3}	0.24	0.26	0.32
Cut-4	$M_T > 1600 \mathrm{GeV}$	1.0×10^{-3}	0.19	0.21	0.25

TABLE VII: The cut-flow table for the off-shell mediator scenario of the \mathcal{L}_3 model with $m_D = 20$ GeV and its relevant background. The three benchmark points are signal-1 $(M/m_D = 1.1)$, signal-2 $(M/m_D = 1.5)$, signal-3 $(M/m_D = 1.9)$.

	Cut description	background	signal1	signal2	signal3
	Cross-section [fb]	2980	0.34	0.36	0.45
	$N(\gamma) > 0$	0.92	0.91	0.91	0.91
Cut-1	$E(\gamma) > 100 \text{GeV} \& \eta(\gamma) < 2.5$	0.35	0.69	0.70	0.74
	$E_T > 40\mathrm{GeV}$	0.30	0.67	0.68	0.72
Cut-2	$E(\gamma) > 1200 \mathrm{GeV}$	7.4×10^{-3}	0.28	0.31	0.43
Cut-3	$P_T(\gamma)/E > 0.4$	1.7×10^{-3}	0.16	0.18	0.26
Cut-4	$M_T > 1600 \mathrm{GeV}$	1.0×10^{-3}	0.13	0.15	0.21

TABLE VIII: Similar to Table VII, but for the \mathcal{L}_3 model with $m_D = 100$ GeV.

for the respective models and masses, while kinematic distributions appear in Figs. 4-9.

Due to off-shell mediator production, significant overlaps may occur between signal and background distributions in $E(\gamma)$, E_T , and E, comparing with the on-shell case in Sec. III B. However, the \mathcal{L}_9 model shows obviously less overlap than the \mathcal{L}_{13} model. Nevertheless, the ratio $P_T(\gamma)/E$ and M_T distributions (defined in Sec. III B) remain effective discriminators except for the \mathcal{L}_{13} model. Applying the same event selections as Sec. III B, we summarize the selection efficiencies in Tables VII-XII for the respective models and masses. The distinguishable kinematics for the \mathcal{L}_9 model yield higher signal efficiencies after all cuts, while the

	Cut description	background	signal1	signal2	signal3
	Cross-section [fb]	2980	0.30	0.42	1.20
	$N(\gamma) > 0$	0.92	0.91	0.91	0.91
Cut-1	$E(\gamma) > 100 \text{GeV} \& \eta(\gamma) < 2.5$	0.35	0.91	0.91	0.91
	$E_T > 40\mathrm{GeV}$	0.30	0.91	0.91	0.91
Cut-2	$E(\gamma) > 1200\mathrm{GeV}$	7.4×10^{-3}	0.91	0.91	0.91
Cut-3	$P_T(\gamma)/E > 0.4$	1.7×10^{-3}	0.57	0.58	0.58
Cut-4	$M_T > 1600 \mathrm{GeV}$	1.0×10^{-3}	0.45	0.46	0.46

TABLE IX: Similar to Table VII, but for the \mathcal{L}_9 model with $m_D=20$ GeV.

Cut description		background	signal1	signal2	signal3
	Cross-section [fb]	2980	1.3×10^{-2}	1.8×10^{-2}	4.9×10^{-2}
	$N(\gamma) > 0$	0.92	0.91	0.91	0.91
Cut-1	$E(\gamma) > 100 \text{GeV} \& \eta(\gamma) < 2.5$	0.35	0.90	0.90	0.91
	$E_T > 40\mathrm{GeV}$	0.30	0.90	0.90	0.91
Cut-2	$E(\gamma) > 1200 \mathrm{GeV}$	7.4×10^{-3}	0.85	0.87	0.90
Cut-3	$P_T(\gamma)/E > 0.4$	1.7×10^{-3}	0.53	0.53	0.56
Cut-4	$M_T > 1600 \mathrm{GeV}$	1.0×10^{-3}	0.42	0.43	0.44

TABLE X: Similar to Table VII, but for the \mathcal{L}_9 model with $m_D = 100$ GeV.

Cut description		background	signal1	signal2	signal3
	Cross-section [fb]	2980	518	533	521
	$N(\gamma) > 0$	0.92	0.91	0.91	0.91
Cut-1	$E(\gamma) > 100 \text{GeV} \& \eta(\gamma) < 2.5$	0.35	0.54	0.54	0.53
	$E_T > 40\mathrm{GeV}$	0.30	0.51	0.50	0.49
Cut-2	$E(\gamma) > 1200\mathrm{GeV}$	7.4×10^{-3}	3.0×10^{-2}	2.8×10^{-2}	3.2×10^{-2}
Cut-3	$P_T(\gamma)/E > 0.4$	1.7×10^{-3}	1.5×10^{-2}	1.6×10^{-2}	1.8×10^{-2}
Cut-4	$M_T > 1600 \mathrm{GeV}$	1.0×10^{-3}	1.3×10^{-2}	1.3×10^{-2}	1.6×10^{-2}

TABLE XI: Similar to Table VII, but for the \mathcal{L}_{13} model with $m_D=20$ GeV.

Cut description		background	signal1	signal2	signal3
Cross-section [fb]		2980	0.83	0.84	0.84
	$N(\gamma) > 0$	0.92	0.91	0.91	0.92
Cut-1	$E(\gamma) > 100 \text{GeV} \& \eta(\gamma) < 2.5$	0.35	0.53	0.53	0.52
	$E_T > 40\mathrm{GeV}$	0.30	0.48	0.49	0.49
Cut-2	$E(\gamma) > 1200\mathrm{GeV}$	7.4×10^{-3}	2.6×10^{-2}	2.7×10^{-2}	3.2×10^{-2}
Cut-3	$P_T(\gamma)/E > 0.4$	1.7×10^{-3}	1.4×10^{-2}	1.4×10^{-2}	1.8×10^{-2}
Cut-4	$M_T > 1600 \mathrm{GeV}$	1.0×10^{-3}	1.3×10^{-2}	1.2×10^{-2}	1.5×10^{-2}

TABLE XII: Similar to Table VII, but for the \mathcal{L}_{13} model with $m_D = 100$ GeV.

nearly identical kinematic distributions between signal and background events for the \mathcal{L}_{13} model pose challenges, resulting in only factor-of-ten signal-background separation. Additionally, signal efficiency increases slightly with M/m_D but remains largely independent of m_D for its value below 100 GeV.

IV. RESULTS AND DISCUSSIONS

After establishing the three search strategies in Sec. III, we determine the efficiencies $(\epsilon_{s,b})$ for both signal and background events. Two specific scenarios required adjustments to the selection criteria. First, for mediator masses near 1500 GeV, the initial requirement of $E(\gamma) > 1200$ GeV in Cut-2 for the search of invisible on-shell mediator decays proved overly restrictive; we therefore relaxed it to $E(\gamma) > 1000$ GeV. Similarly, for the mediator mass close to 20 GeV in the analysis of visible on-shell mediator decays, the pseudorapidity requirements in Cut-2, Cut-3, and the original $p_T(\mu^{\pm}) > 150$ GeV in Cut-3 were found to be overly stringent. Therefore, we relaxed them to $p_T(\mu^{\pm}) > 50$ GeV, $|\eta(\gamma)| < 2.2$, and $|\eta(\mu^{\pm})| < 2.2$, respectively. Moreover, signal and background production cross-sections $(\sigma_{s,b})$ are computed using MadGraph5_aMC@NLO. Additionally, we adopt an optimistic integrated luminosity of L = 4400 fb⁻¹ [82, 83]. The expected numbers of signal and background events are then given by $N_{s,b} = \sigma_{s,b} \times \epsilon_{s,b} \times L$.

After obtaining the signal and background event counts, the signal significance is calcu-

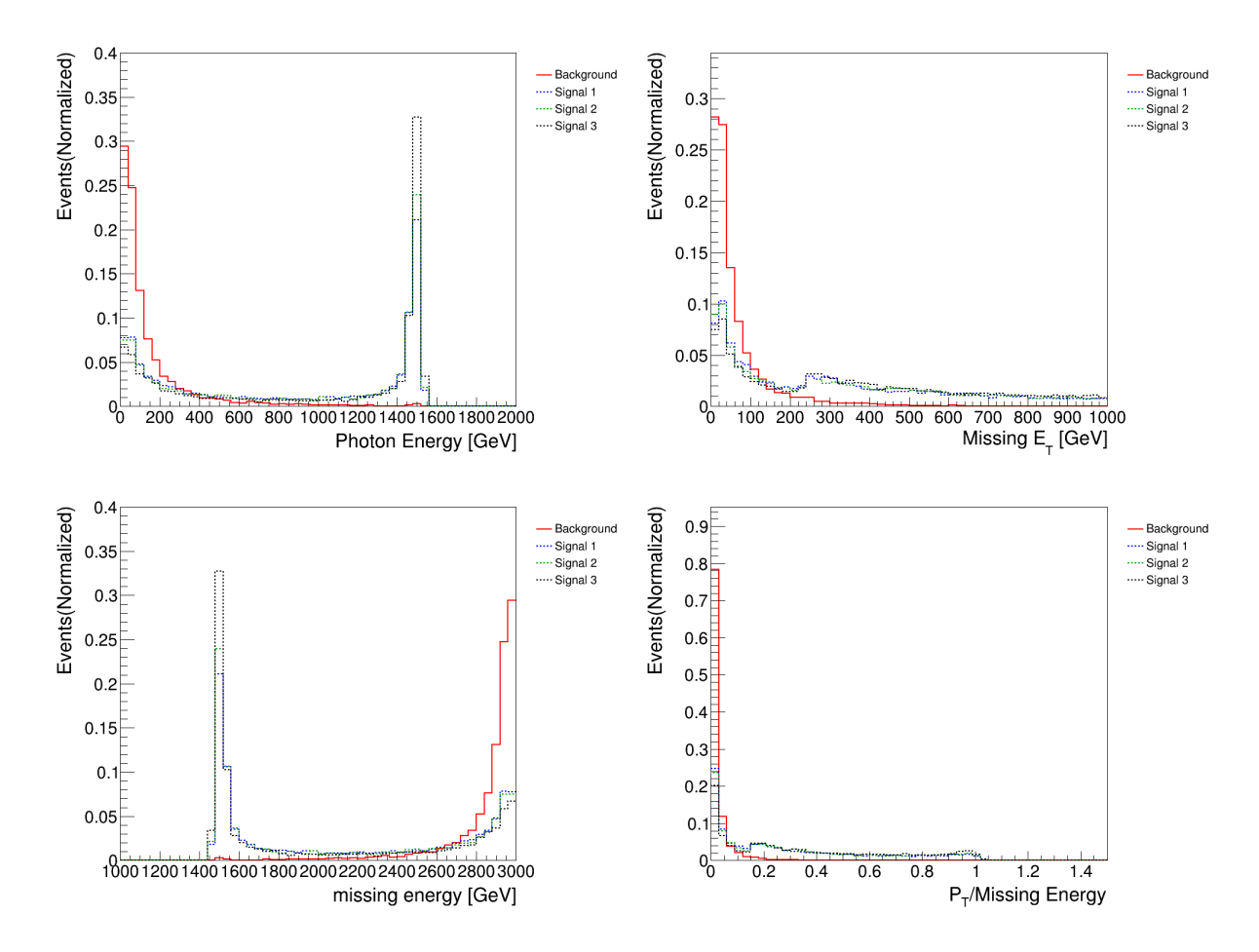


FIG. 4: In the off-shell mediator scenario of the \mathcal{L}_3 model with $m_D = 20$ GeV, representative kinematic distributions include photon energy $E(\gamma)$ (top-left), missing transverse energy E_T (top-right), missing energy E (bottom-left), and the ratio of $P_T(\gamma)/E$ (bottom-right) for signal-1 ($M/m_D = 1.1$, blue-dotted line), signal-2 ($M/m_D = 1.5$, green-dotted line), signal-3 ($M/m_D = 1.9$, black-dotted line), and background (red-solid line).

lated as [84, 85]
$$Z = \sqrt{2 \cdot [(N_s + N_b) \cdot \ln(1 + \frac{N_s}{N_b}) - N_s]}. \tag{3}$$

To account for systematic uncertainties in the background, this formula is modified to [85, 86]

$$Z = \sqrt{2 \cdot \left[(N_s + N_b) \cdot \ln\left[\frac{(N_s + N_b)(N_b + \sigma_b^2)}{N_b^2 + (N_s + N_b)\sigma_b^2} \right] - \frac{N_s^2}{\sigma_b^2} \cdot \ln\left(1 + \frac{N_b \sigma_b^2}{N_s^2 + N_b \sigma_b^2}\right) \right]}.$$
 (4)

In this work, we adopt a conservative estimate for the systematic uncertainty, setting $\sigma_b = 0.05N_b$, which corresponds to 5% of the total background event. Here we use a

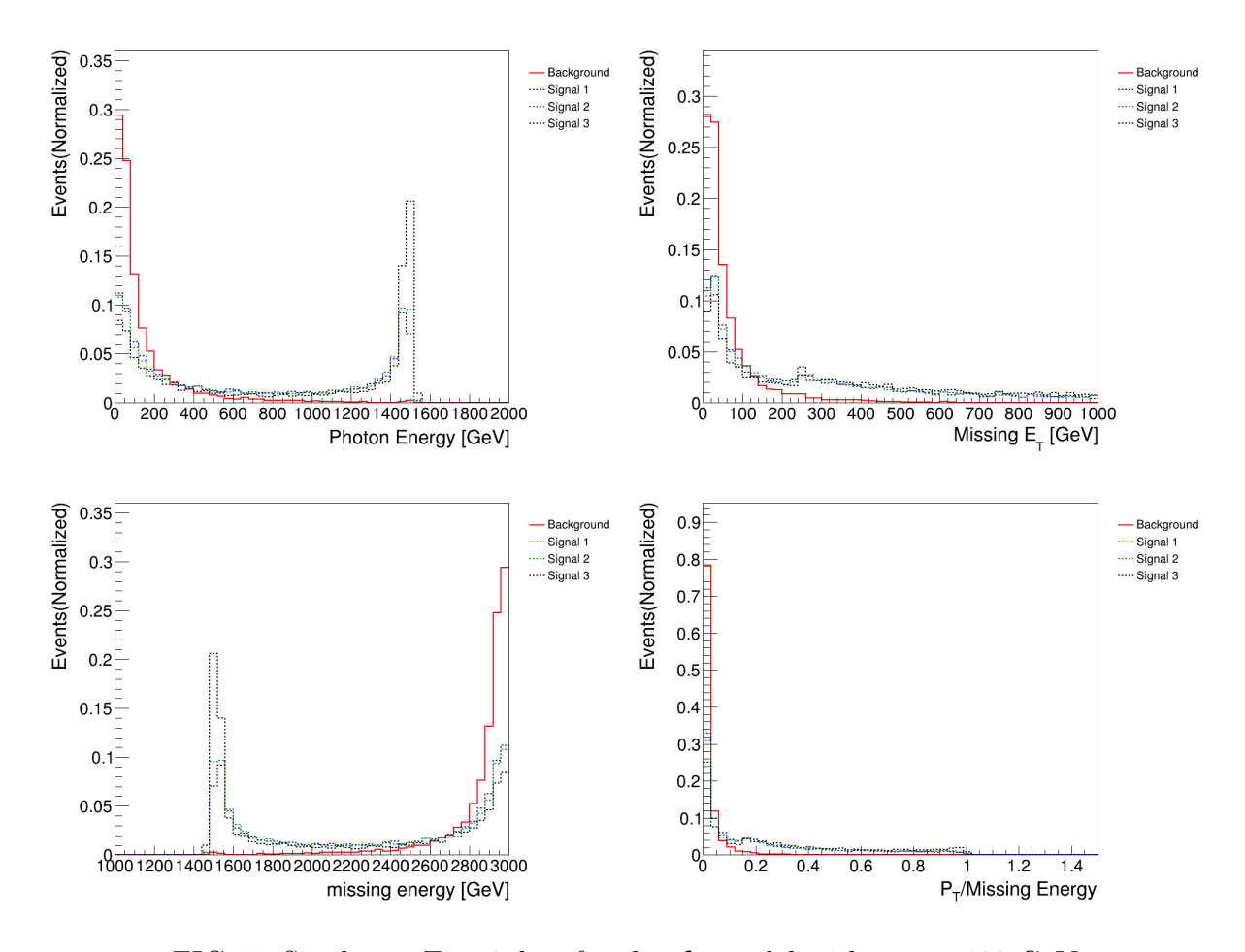


FIG. 5: Similar to Fig. 4, but for the \mathcal{L}_3 model with $m_D = 100$ GeV.

significance threshold of Z=1.96, corresponding to a 95% confidence level, to project the future exclusion limits for \mathcal{L}_3 , \mathcal{L}_4 , \mathcal{L}_8 , \mathcal{L}_9 , \mathcal{L}_{10} , \mathcal{L}_{13} , and \mathcal{L}_{14} at a 3 TeV muon collider.

For visible on-shell mediator decays, we impose the condition $\mathcal{B}(\text{MED} \to \mu^+\mu^-) > 99\%$ to determine the coupling parameter ratios, which in turn fixes g_D/g_f for the \mathcal{L}_3 , \mathcal{L}_4 , and \mathcal{L}_8 models and $M_{D\phi}/g_f$ for the \mathcal{L}_9 , \mathcal{L}_{10} , \mathcal{L}_{13} , and \mathcal{L}_{14} models. These ratios are listed in the third column of Table XIII. We can find that the coupling parameter ratios for four models \mathcal{L}_9 , \mathcal{L}_{10} , \mathcal{L}_{13} , and \mathcal{L}_{14} span a range of values rather than taking a single fixed one. This behavior occurs because the dimension-1 coupling $M_{D\phi}$, which is closely related to the mediator mass for the mediator branching ratio calculations. Specifically, the ratio $M_{D\phi}/g_f$ required to satisfy $\mathcal{B}(\text{MED} \to \mu^+\mu^-) > 99\%$ increases monotonically with the mediator mass. Furthermore, relaxing the branching ratio condition to values below 99% would lead to a decrease in both the g_D/g_f and $M_{D\phi}/g_f$ ratios.

Using a mass ratio of $M/m_D = 2.5$ (ensuring $M > 2m_D$) and benchmark mediator

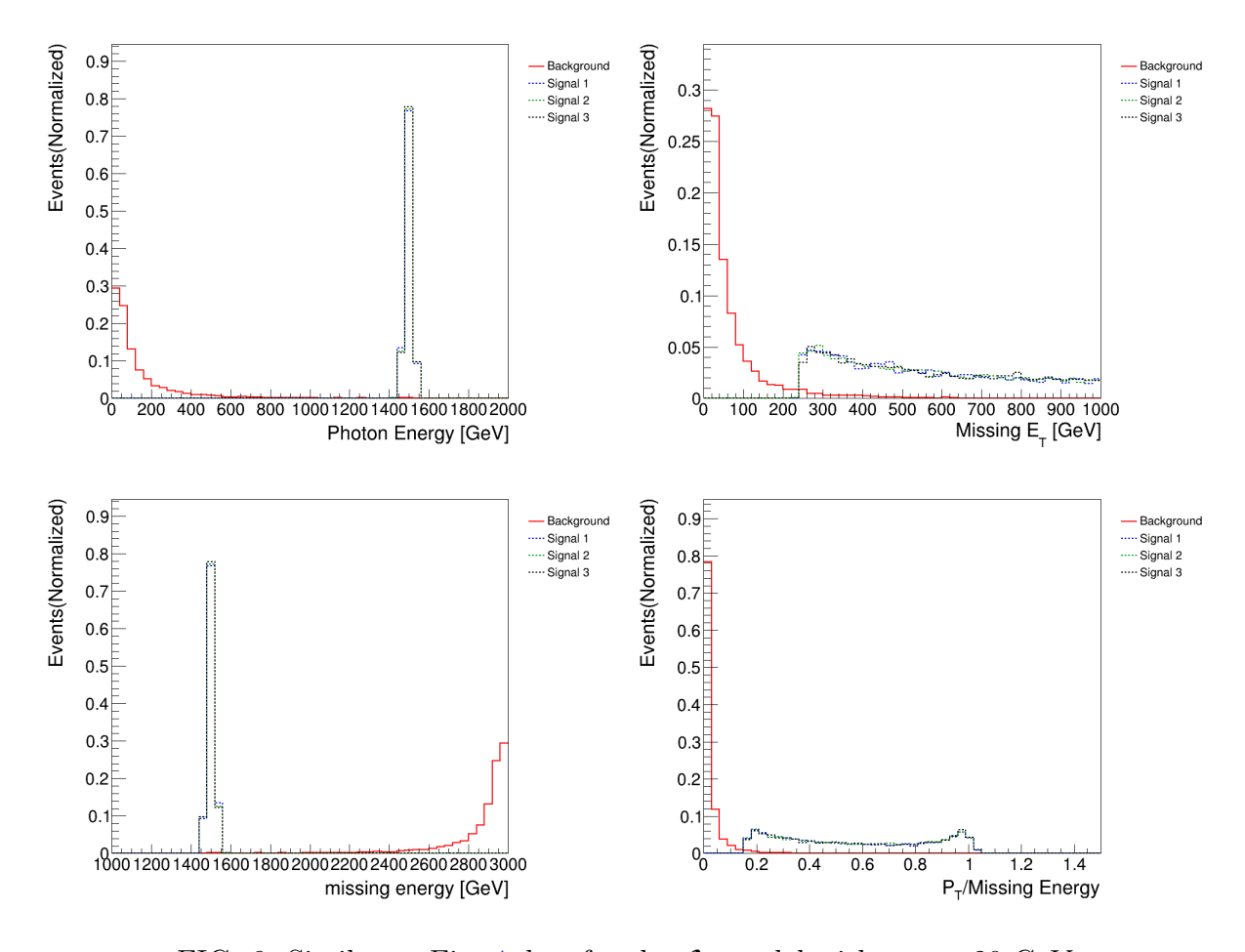


FIG. 6: Similar to Fig. 4, but for the \mathcal{L}_9 model with $m_D = 20$ GeV.

masses M from 20 GeV to 1500 GeV, we derive the projected exclusion limits at significance Z=1.96. Our analysis shows that once the condition $M>2m_D$ is met, the results depend only moderately on the specific value of the M/m_D ratio. The solid and dashed lines in Fig. 10 show these projected exclusion limits without and with 5% systematic uncertainty, respectively. Among them, the exclusion lines of the \mathcal{L}_3 , \mathcal{L}_4 , and \mathcal{L}_8 models decrease monotonically with the increase of the mediator mass M, while those of the \mathcal{L}_9 , \mathcal{L}_{10} , \mathcal{L}_{13} , and \mathcal{L}_{14} models increase with the rise of M. Notably, the latter exhibits a monotonically decreasing trend within the mass range of 20 GeV – 100 GeV. This behaviour arises from the relaxed selection criteria for mediators with M=20 GeV, which increases the background efficiency at the same time to twice its original value; to meet the significance threshold of Z=1.96, the required production cross-section corresponding to M=20 GeV is consequently enhanced. Furthermore, under the standard selection criteria, the signal efficiency for M=50 GeV is only 58% of that for M=100 GeV; thus, the required production

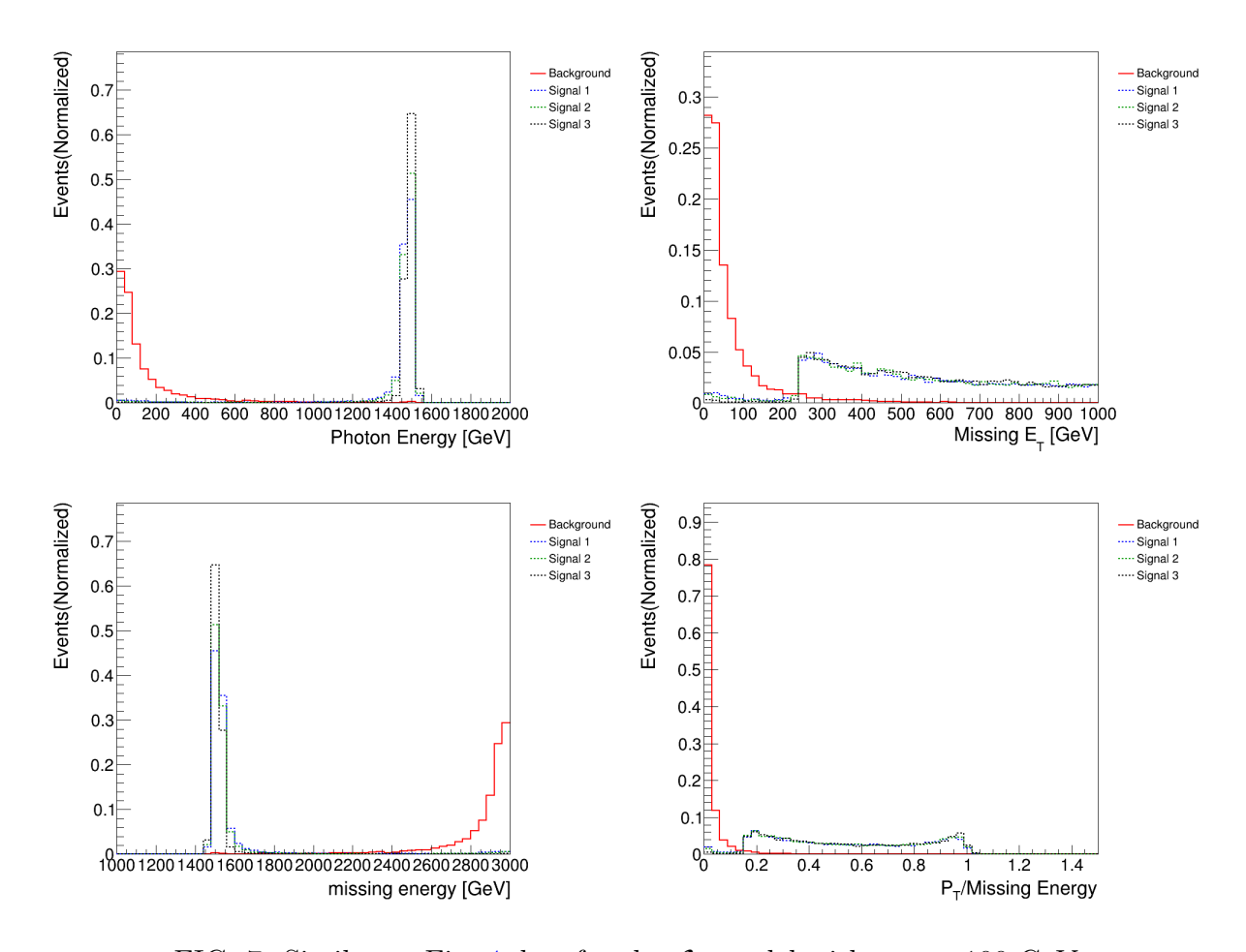


FIG. 7: Similar to Fig. 4, but for the \mathcal{L}_9 model with $m_D = 100$ GeV.

cross-section for M = 50 GeV is also larger than the corresponding value at M = 100 GeV.

The analysis for invisible on-shell mediator decays follows the same workflow but uses the condition $\mathcal{B}(\text{MED} \to \text{DM} + \text{DM}) > 99\%$ to prioritize DM pair production. The corresponding coupling parameter ratios g_D/g_f and $M_{D\phi}/g_f$ are listed in the fourth column of Table XIII. Again, the ratio $M_{D\phi}/g_f$ increases monotonically with the mediator mass for the fixed condition $\mathcal{B}(\text{MED} \to \text{DM} + \text{DM}) > 99\%$. Since the results depend only mildly on the M/m_D ratio once $M > 2m_D$ is satisfied, we fix $M/m_D = 2.5$ and use the same range of benchmark mediator masses. The resulting projected exclusion limits, with and without systematic uncertainty, are shown by the solid and dashed lines in Fig. 11, respectively. In contrast to the visible decay process, the exclusion lines of the \mathcal{L}_3 , \mathcal{L}_4 , and \mathcal{L}_8 models in the invisible decay process exhibit a relatively flat trend with the increase of the mediator mass M, while those of the \mathcal{L}_9 , \mathcal{L}_{10} , \mathcal{L}_{13} , and \mathcal{L}_{14} models increase monotonically as the mediator mass M grows.

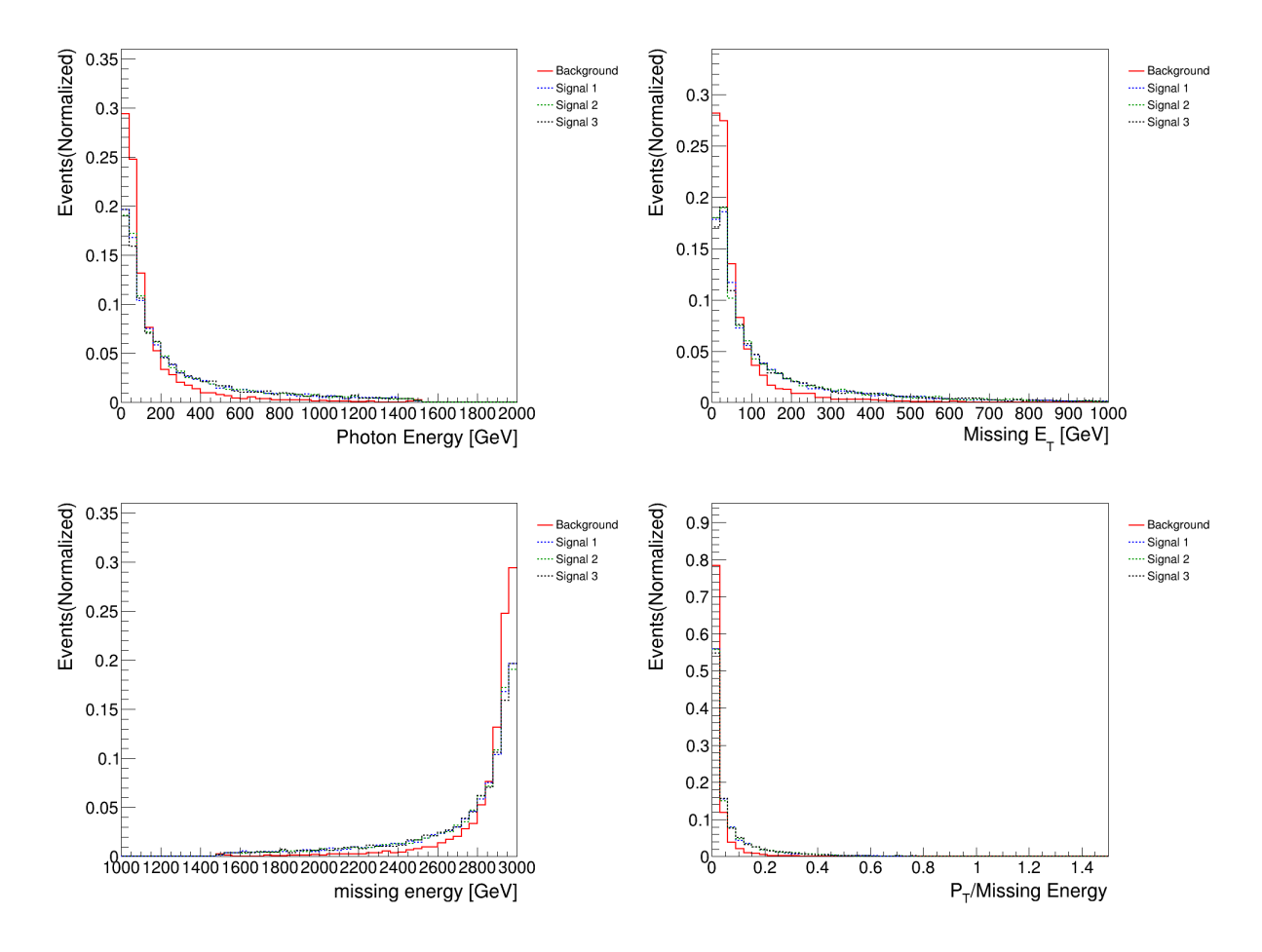


FIG. 8: Similar to Fig. 4, but for the \mathcal{L}_{13} model with $m_D = 20$ GeV.

The exclusion limits derived from visible on-shell mediator decays are consistently stronger than those from invisible on-shell mediator decays across all models. This behavior can be understood for two main reasons. First, the relevant SM background for the visible decay signal process is more than an order of magnitude smaller than for the invisible decay signal process. Second, although the production cross-sections for both signal processes are proportional to g_f^2 , the requirement of a larger than 99% branching ratio to either $\mu^+\mu^-$ or a pair of DM particles results in distinctly different values for the coupling parameter ratios g_D/g_f and $M_{D\phi}/g_f$, as shown in Table XIII.

For the mono-photon channel with an off-shell mediator, the production cross-sections are directly proportional to $g_D \cdot g_f$ for \mathcal{L}_3 , \mathcal{L}_4 , \mathcal{L}_8 models and to $M_{D\phi} \cdot g_f$ for \mathcal{L}_9 , \mathcal{L}_{10} , \mathcal{L}_{13} , \mathcal{L}_{14} models. We consider mass ratios $M/m_D=1.1,1.5,1.9$ (satisfying $M<2m_D$) and benchmark DM masses from 20 GeV to 100 GeV. The projected exclusion limits for this scenario, without and with systematic uncertainty, are presented in Fig. 12. In contrast to

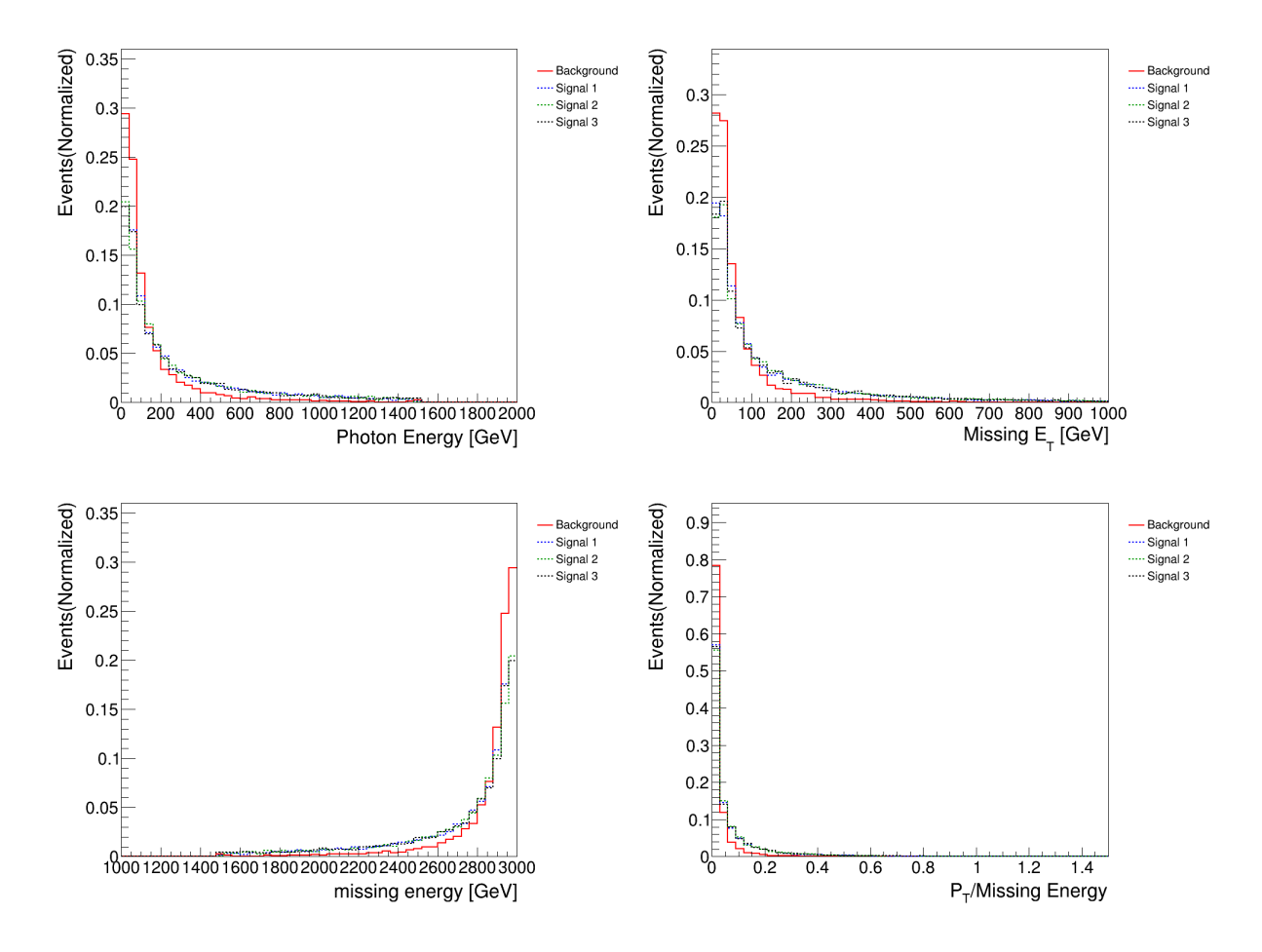


FIG. 9: Similar to Fig. 4, but for the \mathcal{L}_{13} model with $m_D = 100$ GeV.

the on-shell decays, the exclusion lines of all models show a monotonic upward trend with the increase of mediator mass M. Moreover, the larger the mass ratio M/m_D is, the lower the exclusion lines lie, indicating higher detection sensitivity.

In summary, the exclusion limits for the fermionic DM models with scalar or vector mediators (\mathcal{L}_3 , \mathcal{L}_4 , \mathcal{L}_8) reach $\mathcal{O}(10^{-5})$ for $g_D \cdot g_f$ in visible on-shell mediator decays, $\mathcal{O}(10^{-3} - 10^{-2})$ for invisible on-shell mediator decays, and $\mathcal{O}(10^{-2} - 0.1)$ for the mono-photon channel with an off-shell mediator. The projected exclusion contours cover most of the allowed non-resonance regions with $g_D \cdot g_f \gtrsim 10^{-2}$ and mediator masses M between 20 GeV and 1500 GeV for these muonphilic DM models, as shown in Ref. [40]. Similarly, for scalar DM models with a scalar mediator (\mathcal{L}_9 , \mathcal{L}_{10}) and vector DM models with a scalar mediator (\mathcal{L}_{13} , \mathcal{L}_{14}), the exclusion limits on $M_{D\phi}$ (TeV) $\cdot g_f$ reach $\mathcal{O}(10^{-6} - 10^{-5})$ for visible on-shell mediator decays, $\mathcal{O}(10^{-4} - 10^{-2})$ for invisible on-shell mediator. Again, the projected limits cover most

Models	Coupling	Visible on-shell mediator	Invisible on-shell
	parameter	decays	mediator decays
\mathcal{L}_3	g_D/g_f	1/8	15
\mathcal{L}_4	g_D/g_f	1/8	15
\mathcal{L}_8	g_D/g_f	1/9	12
\mathcal{L}_9	$M_{D\phi} ({\rm TeV})/g_f$	$3.66 \times 10^{-3} - 2.75 \times 10^{-1}$	0.91-27.3
\mathcal{L}_{10}	$M_{D\phi} ({\rm TeV})/g_f$	$3.66 \times 10^{-3} - 2.75 \times 10^{-1}$	0.91-27.3
\mathcal{L}_{13}	$M_{D\phi} ({ m TeV})/g_f$	$1.43 \times 10^{-3} - 1.07 \times 10^{-1}$	0.356- 10.68
\mathcal{L}_{14}	$M_{D\phi} ({ m TeV})/g_f$	$1.43 \times 10^{-3} - 1.07 \times 10^{-1}$	0.356- 10.68

TABLE XIII: The ratio of coupling parameters g_D/g_f (for \mathcal{L}_3 , \mathcal{L}_4 , \mathcal{L}_8) and $M_{D\phi}$ (TeV)/ g_f (for \mathcal{L}_9 , \mathcal{L}_{10} , \mathcal{L}_{13} , \mathcal{L}_{14}) used in this analysis for visible on-shell mediator decays with the condition $\mathcal{B}(\text{MED} \to \mu^+\mu^-) > 99\%$ and invisible on-shell mediator decays with the condition $\mathcal{B}(\text{MED} \to \text{DM} + \text{DM}) > 99\%$, respectively.

non-resonance regions with $M_{D\phi}$ (TeV) $\cdot g_f \gtrsim 10^{-4}$ across the same mediator mass range. Therefore, a future 3 TeV muon collider would be critical for testing the muonphilic DM explanation of the GCE puzzle.

V. CONCLUSION

In this work, we have performed a detailed and systematic study of the prospects for discovering muonphilic dark matter (DM) at a future 3 TeV muon collider, focusing on simplified models with a Z_2 -even mediator. Motivated by the model's ability to explain the Galactic Center Excess (GCE) and observed relic density while evading multi-messenger, direct detection and collider constraints, we have explored its viable parameter space through three distinct search channels: visible on-shell mediator decays, invisible on-shell mediator decays, and mono-photon signatures with off-shell mediators.

Our analysis demonstrates that a muon collider possesses exceptional sensitivity to probe the non-resonant regions of these models. For visible on-shell decays, the projected exclusion limits on the fermionic DM model couplings $g_D \cdot g_f$ can reach $\mathcal{O}(10^{-5})$, while for scalar and vector DM models, the limits on $M_{D\phi}$ (TeV) $\cdot g_f$ can be as strong as $\mathcal{O}(10^{-6} - 10^{-5})$.

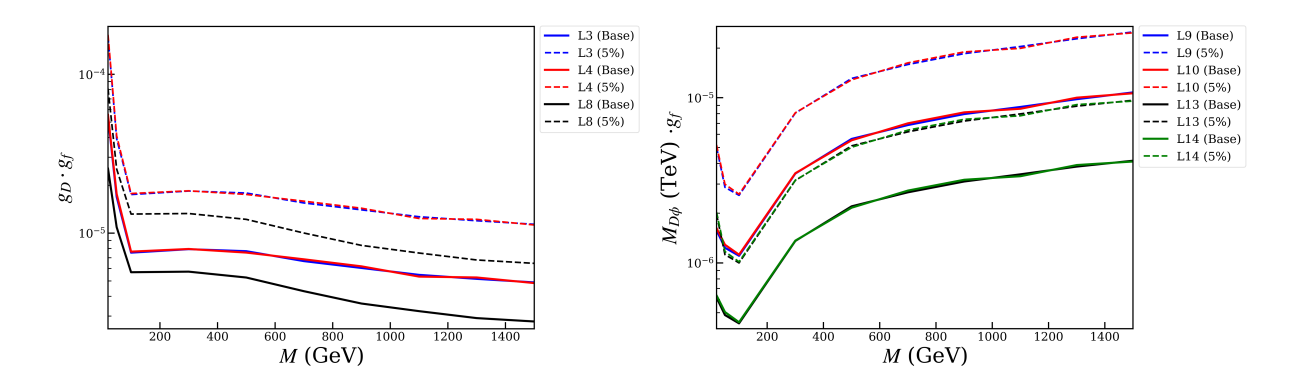


FIG. 10: Projected exclusion limits at 95% confidence level on the parameter space for visible on-shell mediator decays in seven models. The solid and dashed lines correspond to the cases without and with a 5% background systematic uncertainty, respectively. The condition $\mathcal{B}(\text{MED} \to \mu^+\mu^-) > 99\%$ is imposed to determine the ratio of coupling parameters g_D/g_f (for \mathcal{L}_3 , \mathcal{L}_4 , \mathcal{L}_8) and $M_{D\phi}$ (TeV)/ g_f (for \mathcal{L}_9 , \mathcal{L}_{10} , \mathcal{L}_{13} , \mathcal{L}_{14}) as shown in Table XIII.

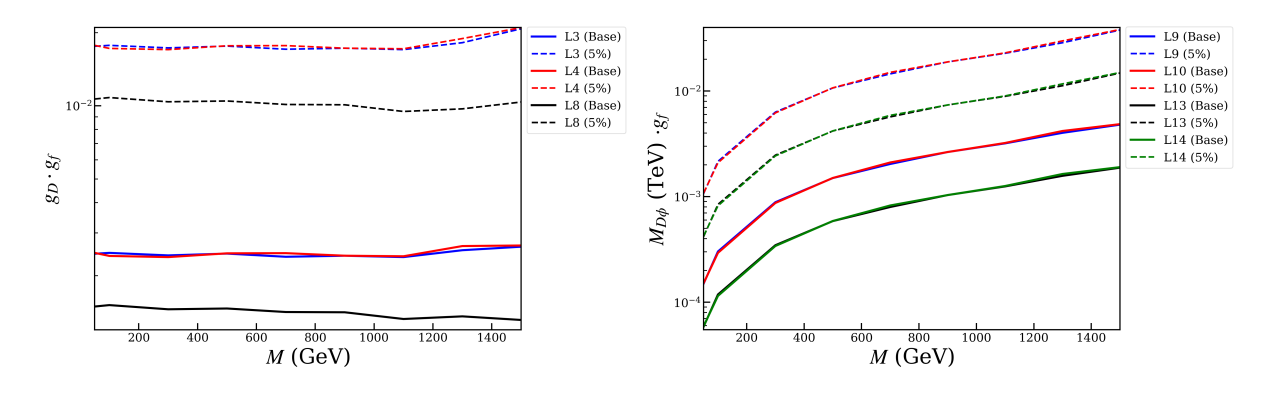


FIG. 11: Similar to Fig. 10, but for invisible on-shell mediator decays in seven models and applying the condition $\mathcal{B}(\text{MED} \to \text{DM} + \text{DM}) > 99\%$ to determine the ratio of coupling parameters.

The invisible on-shell decay channel, while slightly less sensitive due to a larger irreducible background and coupling parameter ratios shown in Table XIII, still provides powerful constraints of $\mathcal{O}(10^{-3}-10^{-2})$ and $\mathcal{O}(10^{-4}-10^{-2})$ for the respective model classes. Furthermore, the mono-photon channel with off-shell mediators offers a complementary probe, especially in parameter regions where $M < 2m_D$, with exclusion limits reaching $\mathcal{O}(10^{-2}-0.1)$ and $\mathcal{O}(10^{-4}-10^{-2})$. We have also quantified the impact of a conservative 5% systematic uncertainty, demonstrating that while it shifts the exclusion limits upward, the projected sen-

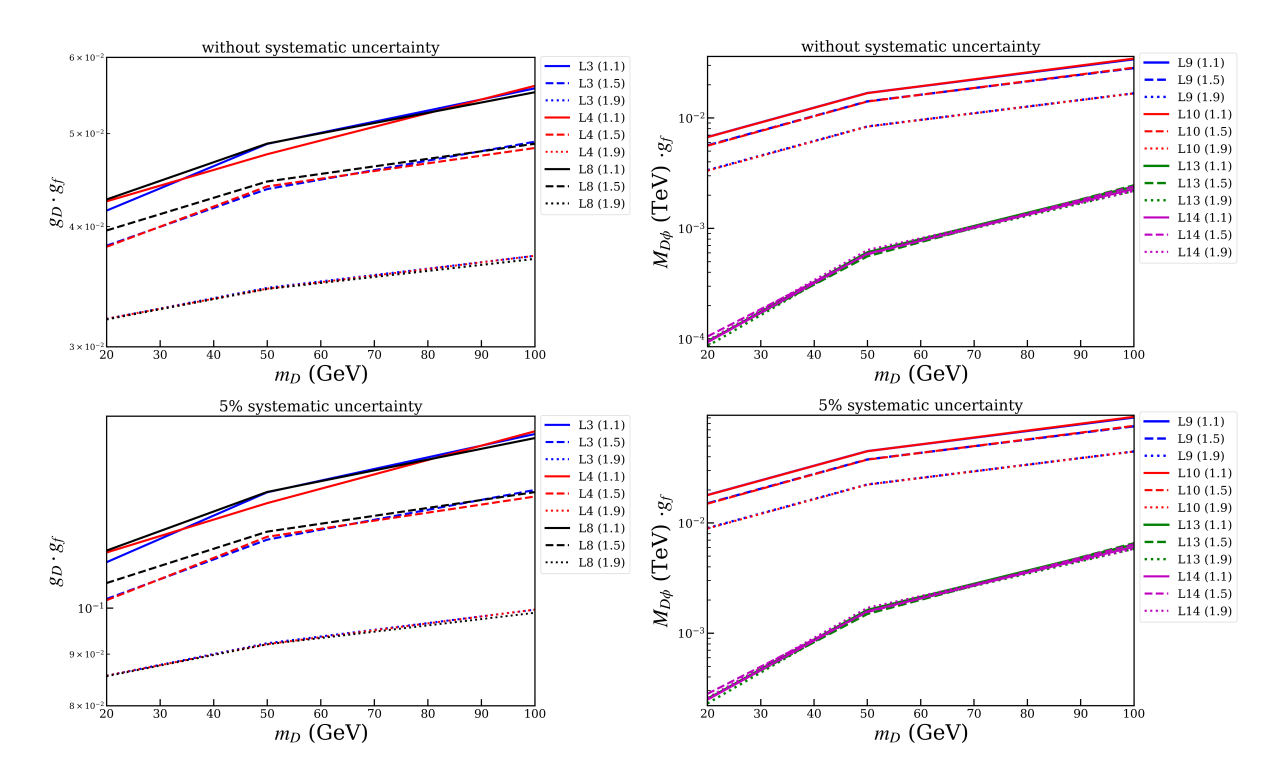


FIG. 12: Projected exclusion limits at 95% confidence level on the parameter space for mono-photon channel with an off-shell mediator in seven models without (top panels) and with a 5% background systematic uncertainty (bottom panels).

sitivity remains substantial. This confirms the robustness of our results. The resulting exclusion contours cover most of the allowed parameter space, specifically for $g_D \cdot g_f \gtrsim 10^{-2}$ and $M_{D\phi} \cdot g_f \gtrsim 10^{-4}$ TeV, across the mediator mass ranges of 20 GeV to 1.5 TeV in the non-resonant regions.

In conclusion, a high-energy muon collider serves as a decisive machine to directly test the muonphilic DM hypothesis as an explanation for the GCE. Its clean collision environment and high luminosity provide a unique opportunity to perform precision measurements of the DM-muon coupling and mediator mass, directly complementing and exceeding the reach of indirect and direct detection experiments as well as conventional collider searches. Our work firmly establishes that such a facility is critical for advancing our understanding of the DM particle nature.

ACKNOWLEDGMENTS

The authors gratefully acknowledge the valuable discussions and insights provided by the members of the China Collaboration of Precision Testing and New Physics. C.T.L., W.Y.C. and H.Q.L. are supported by the National Natural Science Foundation of China (NNSFC) under grants No. 12335005, No. 12575118, and the Special funds for postdoctoral overseas recruitment, Ministry of Education of China.

- [1] V. Trimble, Ann. Rev. Astron. Astrophys. **25**, 425-472 (1987) doi:10.1146/annurev.aa.25.090187.002233
- [2] L. Barack, V. Cardoso, S. Nissanke, T. P. Sotiriou, A. Askar, C. Belczynski, G. Bertone,
 E. Bon, D. Blas and R. Brito, et al. Class. Quant. Grav. 36, no.14, 143001 (2019)
 doi:10.1088/1361-6382/ab0587 [arXiv:1806.05195 [gr-qc]].
- [3] A. Arbey and F. Mahmoudi, Prog. Part. Nucl. Phys. 119, 103865 (2021) doi:10.1016/j.ppnp.2021.103865 [arXiv:2104.11488 [hep-ph]].
- [4] M. Cirelli, A. Strumia and J. Zupan, [arXiv:2406.01705 [hep-ph]].
- [5] M. Battaglieri, A. Belloni, A. Chou, P. Cushman, B. Echenard, R. Essig, J. Estrada, J. L. Feng,B. Flaugher and P. J. Fox, et al. [arXiv:1707.04591 [hep-ph]].
- [6] T. Lin, PoS **333**, 009 (2019) doi:10.22323/1.333.0009 [arXiv:1904.07915 [hep-ph]].
- [7] E. G. M. Ferreira, Astron. Astrophys. Rev. 29, no.1, 7 (2021) doi:10.1007/s00159-021-00135-6
 [arXiv:2005.03254 [astro-ph.CO]].
- [8] A. Belenchia, M. Carlesso, Ö. Bayraktar, D. Dequal, I. Derkach, G. Gasbarri, W. Herr, Y. L. Li, M. Rademacher and J. Sidhu, et al. Phys. Rept. 951, 1-70 (2022) doi:10.1016/j.physrep.2021.11.004 [arXiv:2108.01435 [quant-ph]].
- [9] C. Pérez de los Heros, Symmetry 12, no.10, 1648 (2020) doi:10.3390/sym12101648[arXiv:2008.11561 [astro-ph.HE]].
- [10] T. R. Slatyer, SciPost Phys. Lect. Notes 53, 1 (2022) doi:10.21468/SciPostPhysLectNotes.53
 [arXiv:2109.02696 [hep-ph]].
- [11] I. Cholis, Y. M. Zhong, S. D. McDermott and J. P. Surdutovich, Phys. Rev. D 105, no.10, 103023 (2022) doi:10.1103/PhysRevD.105.103023 [arXiv:2112.09706 [astro-ph.HE]].

- [12] M. Di Mauro and M. W. Winkler, Phys. Rev. D 103, no.12, 123005 (2021) doi:10.1103/PhysRevD.103.123005 [arXiv:2101.11027 [astro-ph.HE]].
- [13] M. Y. Cui, Q. Yuan, Y. L. S. Tsai and Y. Z. Fan, Phys. Rev. Lett. 118, no.19, 191101 (2017) doi:10.1103/PhysRevLett.118.191101 [arXiv:1610.03840 [astro-ph.HE]].
- [14] A. Cuoco, M. Krämer and M. Korsmeier, Phys. Rev. Lett. 118, no.19, 191102 (2017) doi:10.1103/PhysRevLett.118.191102 [arXiv:1610.03071 [astro-ph.HE]].
- [15] F. Calore, M. Cirelli, L. Derome, Y. Genolini, D. Maurin, P. Salati and P. D. Serpico, SciPost Phys. 12, no.5, 163 (2022) doi:10.21468/SciPostPhys.12.5.163 [arXiv:2202.03076 [hep-ph]].
- [16] C. A. Kierans, S. E. Boggs, A. Zoglauer, A. W. Lowell, C. Sleator, J. Beechert, T. J. Brandt, P. Jean, H. Lazar and J. Roberts, et al. Astrophys. J. 895, no.1, 44 (2020) doi:10.3847/1538-4357/ab89a9 [arXiv:1912.00110 [astro-ph.HE]].
- [17] R. G. Cai, Y. C. Ding, X. Y. Yang and Y. F. Zhou, JCAP 03, 057 (2021) doi:10.1088/1475-7516/2021/03/057 [arXiv:2007.11804 [astro-ph.CO]].
- [18] C. Keith and D. Hooper, Phys. Rev. D 104, no.6, 063033 (2021) doi:10.1103/PhysRevD.104.063033 [arXiv:2103.08611 [astro-ph.CO]].
- [19] E. M. Silich, K. Jahoda, L. Angelini, P. Kaaret, A. Zajczyk, D. M. LaRocca, R. Ringuette and J. Richardson, Astrophys. J. 916, no.1, 2 (2021) doi:10.3847/1538-4357/ac043b [arXiv:2105.12252 [astro-ph.HE]].
- [20] D. Hooper and T. R. Slatyer, Phys. Dark Univ. 2, 118-138 (2013) doi:10.1016/j.dark.2013.06.003 [arXiv:1302.6589 [astro-ph.HE]].
- [21] L. Goodenough and D. Hooper, [arXiv:0910.2998 [hep-ph]].
- [22] D. Hooper and L. Goodenough, Phys. Lett. B 697, 412-428 (2011) doi:10.1016/j.physletb.2011.02.029 [arXiv:1010.2752 [hep-ph]].
- [23] A. McDaniel, T. Jeltema, S. Profumo and E. Storm, JCAP 09, 027 (2017) doi:10.1088/1475-7516/2017/09/027 [arXiv:1705.09384 [astro-ph.HE]].
- [24] T. E. Jeltema and S. Profumo, Mon. Not. Roy. Astron. Soc. 421, 1215 (2012) doi:10.1111/j.1365-2966.2011.20382.x [arXiv:1108.1407 [astro-ph.HE]].
- [25] M. Ajello et al. [Fermi-LAT], Astrophys. J. 819, no.1, 44 (2016) doi:10.3847/0004-637X/819/1/44 [arXiv:1511.02938 [astro-ph.HE]].
- [26] J. F. Navarro, C. S. Frenk and S. D. M. White, Astrophys. J. 462, 563-575 (1996) doi:10.1086/177173 [arXiv:astro-ph/9508025 [astro-ph]].

- [27] M. J. Dolan, F. Kahlhoefer, C. McCabe and K. Schmidt-Hoberg, JHEP 03, 171 (2015) [erratum: JHEP 07, 103 (2015)] doi:10.1007/JHEP03(2015)171 [arXiv:1412.5174 [hep-ph]].
- [28] S. Ipek, D. McKeen and A. E. Nelson, Phys. Rev. D 90, no.5, 055021 (2014) doi:10.1103/PhysRevD.90.055021 [arXiv:1404.3716 [hep-ph]].
- [29] A. Berlin, D. Hooper and S. D. McDermott, Phys. Rev. D 89, no.11, 115022 (2014) doi:10.1103/PhysRevD.89.115022 [arXiv:1404.0022 [hep-ph]].
- [30] A. Alves, S. Profumo, F. S. Queiroz and W. Shepherd, Phys. Rev. D 90, no.11, 115003 (2014) doi:10.1103/PhysRevD.90.115003 [arXiv:1403.5027 [hep-ph]].
- [31] P. Agrawal, B. Batell, D. Hooper and T. Lin, Phys. Rev. D 90, no.6, 063512 (2014) doi:10.1103/PhysRevD.90.063512 [arXiv:1404.1373 [hep-ph]].
- [32] E. Izaguirre, G. Krnjaic and B. Shuve, Phys. Rev. D 90, no.5, 055002 (2014) doi:10.1103/PhysRevD.90.055002 [arXiv:1404.2018 [hep-ph]].
- [33] P. Ko, W. I. Park and Y. Tang, JCAP 09, 013 (2014) doi:10.1088/1475-7516/2014/09/013 [arXiv:1404.5257 [hep-ph]].
- [34] M. Abdullah, A. DiFranzo, A. Rajaraman, T. M. P. Tait, P. Tanedo and A. M. Wijangco, Phys. Rev. D 90, 035004 (2014) doi:10.1103/PhysRevD.90.035004 [arXiv:1404.6528 [hep-ph]].
- [35] A. Martin, J. Shelton and J. Unwin, Phys. Rev. D 90, no.10, 103513 (2014) doi:10.1103/PhysRevD.90.103513 [arXiv:1405.0272 [hep-ph]].
- [36] A. Berlin, P. Gratia, D. Hooper and S. D. McDermott, Phys. Rev. D 90, no.1, 015032 (2014) doi:10.1103/PhysRevD.90.015032 [arXiv:1405.5204 [hep-ph]].
- [37] C. Cheung, M. Papucci, D. Sanford, N. R. Shah and K. M. Zurek, Phys. Rev. D 90, no.7, 075011 (2014) doi:10.1103/PhysRevD.90.075011 [arXiv:1406.6372 [hep-ph]].
- [38] P. Agrawal, B. Batell, P. J. Fox and R. Harnik, JCAP 05, 011 (2015) doi:10.1088/1475-7516/2015/05/011 [arXiv:1411.2592 [hep-ph]].
- [39] C. Karwin, S. Murgia, T. M. P. Tait, T. A. Porter and P. Tanedo, Phys. Rev. D 95, no.10, 103005 (2017) doi:10.1103/PhysRevD.95.103005 [arXiv:1612.05687 [hep-ph]].
- [40] M. Abdughani, Y. Z. Fan, C. T. Lu, T. P. Tang and Y. L. S. Tsai, JHEP 07, 127 (2022) doi:10.1007/JHEP07(2022)127 [arXiv:2111.02946 [astro-ph.HE]].
- [41] G. Elor, N. L. Rodd, T. R. Slatyer and W. Xue, JCAP 06, 024 (2016) doi:10.1088/1475-7516/2016/06/024 [arXiv:1511.08787 [hep-ph]].

- [42] M. Di Mauro, Phys. Rev. D 103, no.6, 063029 (2021) doi:10.1103/PhysRevD.103.063029 [arXiv:2101.04694 [astro-ph.HE]].
- [43] R. M. Crocker, N. F. Bell, C. Balazs and D. I. Jones, Phys. Rev. D 81, 063516 (2010) doi:10.1103/PhysRevD.81.063516 [arXiv:1002.0229 [hep-ph]].
- [44] M. H. Chan, Astrophys. Space Sci. 362, no.9, 147 (2017) doi:10.1007/s10509-017-3127-7 [arXiv:1707.00388 [astro-ph.HE]].
- [45] D. Hooper, A. V. Belikov, T. E. Jeltema, T. Linden, S. Profumo and T. R. Slatyer, Phys. Rev. D 86, 103003 (2012) doi:10.1103/PhysRevD.86.103003 [arXiv:1203.3547 [astro-ph.CO]].
- [46] Y. Z. Fan, T. P. Tang, Y. L. S. Tsai and L. Wu, Phys. Rev. Lett. 129, no.9, 091802 (2022) doi:10.1103/PhysRevLett.129.091802 [arXiv:2204.03693 [hep-ph]].
- [47] Y. Z. Fan, Y. Y. Li, C. T. Lu, X. Y. Luo, T. P. Tang, V. Q. Tran and Y. L. S. Tsai, Phys. Rev. D 111, no.1, 015046 (2025) doi:10.1103/PhysRevD.111.015046 [arXiv:2410.00638 [hep-ph]].
- [48] M. Aguilar et al. [AMS], Phys. Rev. Lett. 117, no.9, 091103 (2016) doi:10.1103/PhysRevLett.117.091103
- [49] M. Aguilar et al. [AMS], Phys. Rev. Lett. 122, no.4, 041102 (2019) doi:10.1103/PhysRevLett.122.041102
- [50] Z. Bo et al. [PandaX], Phys. Rev. Lett. 134, no.1, 011805 (2025) doi:10.1103/PhysRevLett.134.011805 [arXiv:2408.00664 [hep-ex]].
- [51] G. Krnjaic, G. Marques-Tavares, D. Redigolo and K. Tobioka, Phys. Rev. Lett. 124, no.4, 041802 (2020) doi:10.1103/PhysRevLett.124.041802 [arXiv:1902.07715 [hep-ph]].
- [52] R. Garani and J. Heeck, Phys. Rev. D 100, no.3, 035039 (2019) doi:10.1103/PhysRevD.100.035039 [arXiv:1906.10145 [hep-ph]].
- [53] M. Drees and W. Zhao, Phys. Lett. B 827, 136948 (2022) doi:10.1016/j.physletb.2022.136948
 [arXiv:2107.14528 [hep-ph]].
- [54] T. Hapitas, D. Tuckler and Y. Zhang, Phys. Rev. D 105, no.1, 016014 (2022) doi:10.1103/PhysRevD.105.016014 [arXiv:2108.12440 [hep-ph]].
- [55] D. Borah, M. Dutta, S. Mahapatra and N. Sahu, Phys. Rev. D 105, no.1, 015029 (2022) doi:10.1103/PhysRevD.105.015029 [arXiv:2109.02699 [hep-ph]].
- [56] A. D. Medina, N. I. Mileo, A. Szynkman and S. A. Tanco, Phys. Rev. D 106, no.7, 075018(2022) doi:10.1103/PhysRevD.106.075018 [arXiv:2112.09103 [hep-ph]].

- [57] J. Heeck and A. Thapa, Eur. Phys. J. C 82, no.5, 480 (2022) doi:10.1140/epjc/s10052-022-10437-3 [arXiv:2202.08854 [hep-ph]].
- [58] S. Baek, J. Kim and P. Ko, JHEP 01, 014 (2025) doi:10.1007/JHEP01(2025)014
 [arXiv:2204.04889 [hep-ph]].
- [59] C. A. Manzari, J. Martin Camalich, J. Spinner and R. Ziegler, Phys. Rev. D 108, no.10, 10 (2023) doi:10.1103/PhysRevD.108.103020 [arXiv:2307.03143 [hep-ph]].
- [60] P. Figueroa, G. Herrera and F. Ochoa, Phys. Rev. D 110, no.9, 095018 (2024) doi:10.1103/PhysRevD.110.095018 [arXiv:2404.03090 [hep-ph]].
- [61] H. Li, Z. Liu and N. Song, [arXiv:2501.06294 [hep-ph]].
- [62] Z. W. Wang, Z. L. Han, F. Huang, Y. Jin and H. Li, Phys. Rev. D 111, no.9, 095017 (2025) doi:10.1103/PhysRevD.111.095017 [arXiv:2501.08622 [hep-ph]].
- [63] T. P. Tang, M. Yang, K. K. Duan, Y. L. S. Tsai and Y. Z. Fan, JCAP 11, 013 (2025) doi:10.1088/1475-7516/2025/11/013 [arXiv:2505.05359 [hep-ph]].
- [64] N. F. Bell, G. Busoni and A. Ghosh, JCAP 10, 060 (2025) doi:10.1088/1475-7516/2025/10/060
 [arXiv:2505.06506 [hep-ph]].
- [65] J. de Blas et al. [Muon Collider], [arXiv:2203.07261 [hep-ph]].
- [66] K. M. Black, S. Jindariani, D. Li, F. Maltoni, P. Meade, D. Stratakis, D. Acosta, R. Agarwal, K. Agashe and C. Aimè, et al. JINST 19, no.02, T02015 (2024) doi:10.1088/1748-0221/19/02/T02015 [arXiv:2209.01318 [hep-ex]].
- [67] C. Accettura, D. Adams, R. Agarwal, C. Ahdida, C. Aimè, N. Amapane, D. Amorim, P. Andreetto, F. Anulli and R. Appleby, et al. Eur. Phys. J. C 83, no.9, 864 (2023) [erratum: Eur. Phys. J. C 84, no.1, 36 (2024)] doi:10.1140/epjc/s10052-023-11889-x [arXiv:2303.08533 [physics.acc-ph]].
- [68] J. M. Cline, G. Dupuis, Z. Liu and W. Xue, JHEP 08, 131 (2014) doi:10.1007/JHEP08(2014)131 [arXiv:1405.7691 [hep-ph]].
- [69] M. Carena, J. Osborne, N. R. Shah and C. E. M. Wagner, Phys. Rev. D 100, no.5, 055002(2019) doi:10.1103/PhysRevD.100.055002 [arXiv:1905.03768 [hep-ph]].
- [70] J. Koechler and M. Di Mauro, [arXiv:2508.02775 [hep-ph]].
- [71] Y. Hu, C. Cesarotti and T. R. Slatyer, [arXiv:2509.08043 [hep-ph]].
- [72] P. A. R. Ade et al. [Planck], Astron. Astrophys. 594, A13 (2016) doi:10.1051/0004-6361/201525830 [arXiv:1502.01589 [astro-ph.CO]].

- [73] Y. Meng et al. [PandaX-4T], Phys. Rev. Lett. 127, no.26, 261802 (2021) doi:10.1103/PhysRevLett.127.261802 [arXiv:2107.13438 [hep-ex]].
- [74] A. Heister *et al.* [ALEPH], Phys. Lett. B **533**, 223-236 (2002) doi:10.1016/S0370-2693(02)01584-8 [arXiv:hep-ex/0203020 [hep-ex]].
- [75] B. Abi et al. [Muon g-2], Phys. Rev. Lett. 126, no.14, 141801 (2021) doi:10.1103/PhysRevLett.126.141801 [arXiv:2104.03281 [hep-ex]].
- [76] P. J. Fox, R. Harnik, J. Kopp and Y. Tsai, Phys. Rev. D 84, 014028 (2011) doi:10.1103/PhysRevD.84.014028 [arXiv:1103.0240 [hep-ph]].
- [77] P. J. Fox, R. Harnik, J. Kopp and Y. Tsai, Phys. Rev. D 85, 056011 (2012) doi:10.1103/PhysRevD.85.056011 [arXiv:1109.4398 [hep-ph]].
- [78] A. Alloul, N. D. Christensen, C. Degrande, C. Duhr and B. Fuks, Comput. Phys. Commun. 185, 2250-2300 (2014) doi:10.1016/j.cpc.2014.04.012 [arXiv:1310.1921 [hep-ph]].
- [79] J. Alwall, R. Frederix, S. Frixione, V. Hirschi, F. Maltoni, O. Mattelaer, H. S. Shao, T. Stelzer,
 P. Torrielli and M. Zaro, JHEP 07, 079 (2014) doi:10.1007/JHEP07(2014)079 [arXiv:1405.0301 [hep-ph]].
- [80] T. Sjöstrand, S. Ask, J. R. Christiansen, R. Corke, N. Desai, P. Ilten, S. Mrenna, S. Prestel, C. O. Rasmussen and P. Z. Skands, Comput. Phys. Commun. 191, 159-177 (2015) doi:10.1016/j.cpc.2015.01.024 [arXiv:1410.3012 [hep-ph]].
- [81] J. de Favereau et al. [DELPHES 3], JHEP 02, 057 (2014) doi:10.1007/JHEP02(2014)057
 [arXiv:1307.6346 [hep-ex]].
- [82] J. P. Delahaye, M. Diemoz, K. Long, B. Mansoulié, N. Pastrone, L. Rivkin, D. Schulte, A. Skrinsky and A. Wulzer, [arXiv:1901.06150 [physics.acc-ph]].
- [83] K. Long, D. Lucchesi, M. Palmer, N. Pastrone, D. Schulte and V. Shiltsev, Nature Phys. 17, no.3, 289-292 (2021) doi:10.1038/s41567-020-01130-x [arXiv:2007.15684 [physics.acc-ph]].
- [84] A. L. Read, J. Phys. G 28, 2693-2704 (2002) doi:10.1088/0954-3899/28/10/313
- [85] A. Arhrib, K. Cheung and C. T. Lu, Phys. Rev. D 102, no.9, 095026 (2020) doi:10.1103/PhysRevD.102.095026 [arXiv:1910.02571 [hep-ph]].
- [86] K. Cheung and C. J. Ouseph, Phys. Rev. D 108, no.3, 035003 (2023) doi:10.1103/PhysRevD.108.035003 [arXiv:2303.16514 [hep-ph]].